Editors' Suggestion

Localized interlayer complexes in heterobilayer transition metal dichalcogenides

M. Danovich,[1] D. A. Ruiz-Tijerina,[1] R. J. Hunt,[2] M. Szyniszewski,[2] N. D. Drummond,[2] and V. I. Fal'ko[1]
[1]*National Graphene Institute, University of Manchester, Booth St E, Manchester M13 9PL, United Kingdom*
[2]*Department of Physics, Lancaster University, Lancaster LA1 4YB, United Kingdom*

(Received 16 February 2018; published 31 May 2018)

We present theoretical results for the radiative rates and doping-dependent photoluminescence spectrum of interlayer excitonic complexes localized by donor impurities in $MoSe_2/WSe_2$ twisted heterobilayers, supported by quantum Monte Carlo calculations of binding energies and wave-function overlap integrals. For closely aligned layers, radiative decay is made possible by the momentum spread of the localized complexes' wave functions, resulting in radiative rates of a few μs^{-1}. For strongly misaligned layers, the short-range interaction between the carriers and impurity provides a finite radiative rate with a strong asymptotic twist angle dependence $\propto\theta^{-8}$. Finally, phonon-assisted recombination is considered, with emission of optical phonons in both layers resulting in additional, weaker emission lines, redshifted by the phonon energy.

DOI: 10.1103/PhysRevB.97.195452

I. INTRODUCTION

Recent advances in the study of two-dimensional (2D) materials have allowed the realization of van der Waals (vdW) heterostructures consisting of vertically stacked 2D layers, resulting in unique properties and potential novel device applications [1–5]. The layers forming these heterostructures are only weakly bound by vdW forces, and largely retain their individual characteristic properties. Yet, the weak interlayer coupling allows the different properties of various 2D materials to be combined.

One such family of vdW heterostructures are heterobilayers of 2D transition metal dichalcogenides (TMDs), which have attracted much interest due to their unique optical properties, dominated by strongly bound excitonic complexes [6,7] and spin- and valley-dependent optical selection rules [8,9]. The most commonly studied heterobilayers are of the form MoX_2/WX_2, with X = S or Se, due to their type-II (staggered) band alignment, in which the lowest conduction-band (CB) edge and the highest valence-band (VB) edge are spatially confined to different layers [10,11]. In this configuration, electrostatic interactions between electrons and holes across the heterostructure result in the formation of interlayer excitonic complexes, whose constituent carriers are spatially separated in the out-of-plane direction. Optical signatures of these interlayer complexes have been reported in photoluminescence (PL) experiments [12–14], where new PL peaks are observed in the spectra of bilayer regions. These signatures appear at energies below the monolayer photoemission lines, due to the smaller interlayer band gap in the staggered band configuration.

Photoemission by free interlayer excitons is limited by the relative interlayer angle θ and the incommensurability of the two TMD lattices δ, resulting in a momentum-space mismatch $\Delta K \approx K\sqrt{\delta^2+\theta^2}$ between the conduction- and valence-band edges, as shown in Fig. 2(b). Radiative recombination becomes effectively indirect, and thus suppressed by energy and momentum conservation [15]. These constraints are relaxed when interlayer excitons and larger excitonic complexes localize about charged defects, such as donor ions, which are commonly observed as dopants in real samples. Formation of these complexes is favored by the long interlayer exciton lifetimes resulting from the spatial separation of their carriers, which allow for their localization by the deep potential wells provided by the ions. The spread in momentum space of these localized complexes opens the possibility for a finite radiative matrix element $M \propto \int d^2r\, e^{i\Delta\mathbf{K}\cdot\mathbf{r}}\Psi(\mathbf{r})$, where $\Psi(\mathbf{r})$ is the envelope wave function of the complex.

In this paper, we provide a theory for the radiative recombination of localized interlayer complexes in TMD heterostructures of the form Mo_2X/WX_2, where the carriers are bound to a donor ion in the MoX_2 layer. Focusing specifically on $MoSe_2/WSe_2$ encapsulated in hexagonal boron nitride (hBN), we use variational and diffusion quantum Monte Carlo (VMC and DMC) simulations [16,17] to evaluate the binding energies and wave-function overlap integrals of complexes involving one or two holes in the WSe_2 layer and up to four electrons in the $MoSe_2$ layer, accounting for bilayer and encapsulation screening effects. We discuss the energetics and stability of these complexes based on their binding energies, and the robustness of our results against uncertainty in model parameters, such as the carrier effective masses and screening lengths.

Motivated by the binding energies obtained from our quantum Monte Carlo (QMC) calculations and PL experiments [18], we study the radiative recombination of the two simplest complexes consisting of MoX_2 electrons and a single WX_2 hole bound to an impurity center: a donor ion and an exciton ($D^0_{c'}h_v$), and a donor-bound trion ($D^0_{c'}X_{vc'}$). We predict the qualitative PL spectrum from these complexes for closely aligned TMD heterobilayers, and estimate the asymptotic behavior of their PL signals in the regime of strong misalignment based on general kinematics and perturbation theory. Our results indicate a rapid decay of the PL signals from the most relevant donor-bound interlayer complexes with the interlayer twist angle (θ), resulting from the asymptotic behavior $\Gamma \sim \theta^{-8}$ of

the radiative rates at strong misalignment. As a consequence, we expect that optical signatures from these complexes can be detected only in closely aligned crystals. Our results provide a new perspective for the interpretation of recently reported luminescence spectra of closely-aligned TMD heterobilayers, where the interlayer portion of the spectrum has been attributed to delocalized interlayer exciton states [12].

The remainder of this paper is organized as follows. In Sec. II, we discuss the model Hamiltonian for the TMD heterobilayer, describe our approach to calculating its optical properties, and present our DMC results for the binding energies of the main interlayer impurity-bound complexes. In Sec. III, we address the PL signatures of these complexes, assuming good alignment between the TMD monolayers in the heterostructure, and estimate the asymptotic behavior of their radiative decay with twist angle in Sec. IV. We consider the effects of electron-phonon interactions in Sec. V, and we find that longitudinal optical phonon modes can introduce redshifted replicas to the main PL lines. Finally, we estimate the evolution of the PL spectrum of the two main donor-bound interlayer complexes with doping in Sec. VI. Our conclusions are summarized in Fig. 1, and discussed in Sec. VII.

II. MODEL

A. Electrostatic interactions in a bilayer system

The reduced dimensionality of a monolayer TMD leads to modified electrostatic interactions between its charge carriers below a characteristic length scale $r_* = 2\pi\kappa/\epsilon$ (in Gaussian units), determined by the monolayer's in-plane dielectric susceptibility κ, and the (average) dielectric constant ϵ of its environment [19,20]. In a TMD heterobilayer, further screening effects must be considered. The resulting interactions between same-layer carriers $\mathcal{V}$ in one layer and $\mathcal{V}'$ in the other, and the interlayer interaction $\mathcal{W}$, have Fourier components (Appendix A)

$$\mathcal{V}(\mathbf{q}) = \frac{2\pi(1 + r'_* q - r'_* q e^{-2qd})}{\epsilon q[(1 + r_* q)(1 + r'_* q) - r_* r'_* q^2 e^{-2qd}]}, \quad (1a)$$

$$\mathcal{V}'(\mathbf{q}) = \frac{2\pi(1 + r_* q - r_* q e^{-2qd})}{\epsilon q[(1 + r_* q)(1 + r'_* q) - r_* r'_* q^2 e^{-2qd}]}, \quad (1b)$$

$$\mathcal{W}(\mathbf{q}) = \frac{2\pi\, e^{-qd}}{\epsilon q[(1 + r_* q)(1 + r'_* q) - r_* r'_* q^2 e^{-2qd}]}, \quad (1c)$$

where $\mathbf{q}$ is the wave vector, d is the interlayer distance, and r_* and r'_* are the corresponding monolayer screening lengths.

Previous works on monolayer TMDs have focused on interactions of the Keldysh form [19] to study their excitonic spectra and optical properties [6,20–23]. For bilayers, this potential form is obtained from Eqs. (1a)–(1c) in the long-range limit ($q \ll 1/r_*, 1/r'_*$) as

$$\mathcal{V}_<(\mathbf{q}) = \mathcal{V}'_<(\mathbf{q}) = \frac{2\pi}{\epsilon q[1 + (r_* + r'_*)q]}, \quad (2a)$$

$$\mathcal{W}_<(\mathbf{q}) = \frac{2\pi}{\epsilon q[1 + (r_* + r'_* + d)q]}. \quad (2b)$$

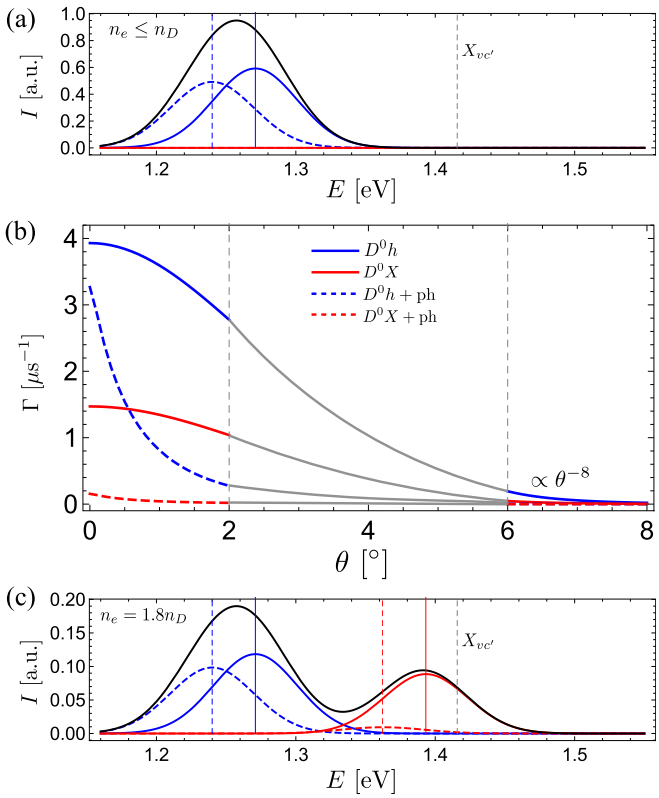

FIG. 1. (a) Simulated PL spectrum of donor-bound interlayer complexes in an aligned ($\theta = 0$) $MoSe_2/WSe_2$ bilayer encapsulated in hexagonal boron nitride, for an electron density of $n_e = 0.9n_D$, with n_D being the donor density. Dashed lines indicate PL from phonon-assisted recombination. Solid lines are taken to have Gaussian shape with width $2\sigma = 60$ meV, and the interlayer gap is $\tilde{E}_g = 1.5$ eV. The vertical gray dashed lines in (a) and (c) indicate the position of the free interlayer exciton $X_{vc'}$. (b) Radiative rates of the $D^0_{c'}h_v$ (per hole) (solid blue) and $D^0_{c'}X_{vc'}$ (solid red) complexes, and their phonon-assisted replicas (dashed), in the large and small twist angle (θ) limits. The rates have a strong angular dependence, with asymptotic behavior $\sim\theta^{-8}$ for radiative decay driven by short-range interactions, and $\sim\theta^{-4}$ for phonon-assisted processes. The gray lines for intermediate twist angles $\theta = 2$–$6°$ have been interpolated by hand. (c) Simulated PL spectrum in the limit of heavy n doping, showing the appearance of the donor-bound trion ($D^0_{c'}X_{vc'}$) line when $n_e > n_D$. Parameters: $n_h = 10^{11}$ cm^{-2} and $n_D = 10^{13}$ cm^{-2}.

By contrast, in the short-range limit ($q \gg 1/r_*, 1/r'_*$) we obtain for the intralayer interactions

$$\mathcal{V}_>(\mathbf{q}) = \frac{2\pi}{\epsilon\, r_* q^2}, \quad \mathcal{V}'_>(\mathbf{q}) = \frac{2\pi}{\epsilon\, r'_* q^2}, \quad (3)$$

revealing the absence of screening from the opposite layer in this regime. More strikingly, the short-range interlayer potential vanishes exponentially as $\mathcal{W}_>(\mathbf{q}) = 2\pi\, e^{-qd}/(\epsilon\, r_* r'_* q^3)$. Neither of these features is captured by extrapolation of Eqs. (2a) and (2b) to large wave numbers.

B. Photon emission by donor-bound complexes

As in the monolayer case [24–27], optical properties of the heterobilayer are determined by excitonic complexes

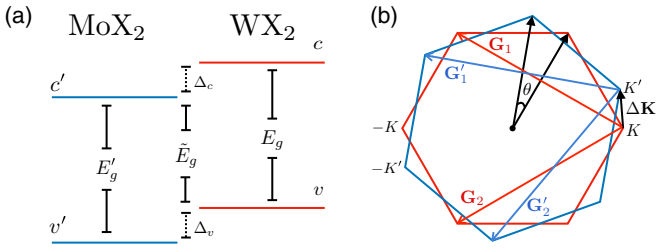

FIG. 2. (a) Schematic of type-II band alignment in a TMD heterobilayer. The CB and VB of the two layers are shifted relative to each other by energies Δ_c and Δ_v, respectively, giving an interlayer gap of $\tilde{E}_g$. (b) The Brillouin zones (BZs) of the misaligned TMD monolayers, with $\mathbf{G}_n$ and $\mathbf{G}'_n$ their main reciprocal lattice vectors. Their K valleys are separated by a momentum vector $\Delta\mathbf{K}$, due to the nonzero misalignment angle θ and to the difference in lattice constants.

formed by excess electrons and holes in the sample. Staggered (type-II) band alignment, in which the main electron and hole bands belong to opposite layers, is typical of TMD heterostructures [10]. This is shown schematically in Fig. 2(a) for a MoX_2/WX_2 structure, where $X = S$ or Se represents a chalcogen; the main electron and hole bands are labeled c' and v, respectively, and the primed (unprimed) band labels correspond to the MoX_2 (WX_2) layer. Given the reduced band gap $\tilde{E}_g$ [Fig. 2(a)], the lowest-energy exciton states are spread across the heterostructure, formed by c'-band electrons and v-band holes bound by the interaction $\mathcal{W}(\mathbf{q})$ [12,13,28].

The optical activity of interlayer excitons in TMD bilayers is strongly constrained by the interlayer alignment. As shown in Fig. 2(b), the relative twist angle and lattice incommensurability between the two layers produces a mismatch between their Brillouin zones (BZs). Thus, bright interlayer excitons in MoX_2/WX_2 structures, consisting of same-valley c'-band electrons and v-band holes, have a finite center-of-mass momentum $\Delta\mathbf{K} = \mathbf{K}' - \mathbf{K}$. Due to energy and momentum conservation, photon emission by interlayer excitons is only allowed when [29] $\Delta K \approx 0$.

The above restrictions are relaxed when excitons and other excitonic complexes are bound to impurity centers in the sample, such as charged defects and donor ions. These complexes are localized within some characteristic length a_0^*, the Bohr radius of the complex, such that their momentum-space wave functions are finite up to momenta of order $1/a_0^*$. As a result, the recombination rates of impurity-bound interlayer complexes are determined by the large-momentum tail of their wave function, and thus by the short-range interaction [Eq. (3)].

The Hamiltonian for the heterobilayer in the free-carrier basis is

$$\hat{H} = \hat{H}_0 + \hat{H}_t + \hat{U}_{\text{intra}} + \hat{U}_{\text{inter}}, \tag{4}$$

where the zeroth-order Hamiltonian $\hat{H}_0$, describing the CB and VB electrons of the two individual layers, is given in second quantization as

$$\hat{H}_0 = \sum_{\alpha} \sum_{\mathbf{k},\tau,\sigma} E_\alpha(\mathbf{k}) c^\dagger_{\alpha,\tau,\sigma}(\mathbf{k}) c_{\alpha,\tau,\sigma}(\mathbf{k}). \tag{5}$$

$c^\dagger_{\alpha,\tau,\sigma}(\mathbf{k})$ creates an electron of spin projection $\sigma = \uparrow,\downarrow$ and momentum $\mathbf{k}$ relative to the $\tau\mathbf{K}$ valley ($\tau = \pm$) of band $\alpha = c', v', c, v$. The band dispersions are

$$E_{v'}(\mathbf{k}) = -\Delta_v - \frac{\hbar^2 k^2}{2m'_v}, \tag{6a}$$

$$E_v(\mathbf{k}) = -\frac{\hbar^2 k^2}{2m_v}, \tag{6b}$$

$$E_{c'}(\mathbf{k}) = \tilde{E}_g + \frac{\hbar^2 k^2}{2m_{c'}}, \tag{6c}$$

$$E_c(\mathbf{k}) = \tilde{E}_g + \Delta_c + \frac{\hbar^2 k^2}{2m_c}, \tag{6d}$$

where Δ_c (Δ_v) is the spacing between the electron (hole) band edges [Fig. 2(a)].

The tunneling Hamiltonian, describing electron hopping between the layers, is given by [30,31]

$$\begin{aligned}\hat{H}_t = \sum_{\tau,\sigma} \sum_{\mathbf{G},\mathbf{G}'} \sum_{\mathbf{k},\mathbf{k}'} \delta_{\tau\mathbf{K}+\mathbf{k}+\mathbf{G},\tau'\mathbf{K}'+\mathbf{k}'+\mathbf{G}'} e^{-i\mathbf{G}_0\cdot\mathbf{r}_0} \\ \times [t_{cc}(\mathbf{k}+\tau\mathbf{K}+\mathbf{G}) c^\dagger_{c\tau\sigma}(\mathbf{k}) c_{c'\tau'\sigma}(\mathbf{k}') \\ + t_{vv}(\mathbf{k}+\tau\mathbf{K}+\mathbf{G}) c^\dagger_{v\tau\sigma}(\mathbf{k}) c_{v'\tau'\sigma}(\mathbf{k}')] + \text{H.c.},\end{aligned} \tag{7}$$

where $t_{cc}(\mathbf{k})$ and $t_{vv}(\mathbf{k})$ represent interlayer hopping strengths between the CBs and VBs; $\mathbf{G}$ and $\mathbf{G}'$ correspond to the reciprocal lattice vectors of the hole and electron layers; and the Kronecker delta enforces momentum conservation in the tunnelling process. $\mathbf{r}_0$ is a vector within the unit cell representing the in-plane shift between the metal atoms of the two TMD monolayers, such that a general stacking configuration is parameterized by $\mathbf{r}_0$ and θ. We focus on configurations with close angular alignment but general $\mathbf{r}_0$; this is a type of pseudo "AA" stacking better suited to describe experimental situations. Correspondingly, we use the *ab initio* hopping terms reported in Ref. [31] for AA stacked ($\mathbf{r}_0 = 0, \theta = 0$) MoS_2, for estimation purposes. These values are small (a few meV) compared to all other scales in the problem, reflecting the vdW and electrical quadrupole nature of the interlayer interactions. As a result, $\hat{H}_t$ can be treated within perturbation theory. Furthermore, since $t_{\alpha\alpha}(\mathbf{k})$ decays rapidly with k, we truncate the sums over $\mathbf{G}$ and $\mathbf{G}'$ to the two main Bragg vectors [31] [Fig. 2(b)], and set $t_{cc}(\tau\mathbf{K}) \approx t_{cc} = 2.5$ meV and $t_{vv}(\tau\mathbf{K}) \approx t_{vv} = 16$ meV.

Finally, the direct electrostatic interactions between carriers, and between carriers and a positive donor ion of effective

charge Z_{donor}, are given by

$$\hat{U}_{\text{intra}} = \frac{e^2}{S}\sum_{\substack{\tau_1,\tau_2\\ \sigma_1,\sigma_2}}\sum_{\mathbf{k}_1,\mathbf{k}_2,\boldsymbol{\xi}}\Bigg[\sum_{\alpha,\beta=v,c}\frac{\mathcal{V}(\boldsymbol{\xi})}{(1+\delta_{\alpha,\beta})}c^\dagger_{\alpha,\tau_1,\sigma_1}(\mathbf{k}_1+\boldsymbol{\xi})c^\dagger_{\beta,\tau_2,\sigma_2}(\mathbf{k}_2-\boldsymbol{\xi})c_{\beta,\tau_2,\sigma_2}(\mathbf{k}_2)c_{\alpha,\tau_1,\sigma_1}(\mathbf{k}_1)$$
$$+\sum_{\alpha,\beta=v',c'}\frac{\mathcal{V}'(\boldsymbol{\xi})}{(1+\delta_{\alpha,\beta})}c^\dagger_{\alpha,\tau_1,\sigma_1}(\mathbf{k}_1+\boldsymbol{\xi})c^\dagger_{\beta,\tau_2,\sigma_2}(\mathbf{k}_2-\boldsymbol{\xi})c_{\beta,\tau_2,\sigma_2}(\mathbf{k}_2)c_{\alpha,\tau_1,\sigma_1}(\mathbf{k}_1)\Bigg]$$
$$-\frac{Z_{\text{donor}}e^2}{S}\sum_{\tau,\sigma}\sum_{\mathbf{k},\boldsymbol{\xi}}\sum_{\alpha=v',c'}\mathcal{V}'(\boldsymbol{\xi})c^\dagger_{\alpha,\tau,\sigma}(\mathbf{k}+\boldsymbol{\xi})c_{\alpha,\tau,\sigma}(\mathbf{k}), \tag{8a}$$

$$\hat{U}_{\text{inter}} = \frac{e^2}{S}\sum_{\substack{\tau_1,\tau_2\\ \sigma_1,\sigma_2}}\sum_{\mathbf{k}_1,\mathbf{k}_2,\boldsymbol{\xi}}\sum_{\alpha=v,c}\sum_{\beta=v',c'}\mathcal{W}(\boldsymbol{\xi})\,c^\dagger_{\alpha,\tau_1,\sigma_1}(\mathbf{k}_1+\boldsymbol{\xi})c^\dagger_{\beta,\tau_2,\sigma_2}(\mathbf{k}_2-\boldsymbol{\xi})c_{\beta,\tau_2,\sigma_2}(\mathbf{k}_2)c_{\alpha,\tau_1,\sigma_1}(\mathbf{k}_1)$$
$$-\frac{Z_{\text{donor}}e^2}{S}\sum_{\tau,\sigma}\sum_{\mathbf{k},\boldsymbol{\xi}}\sum_{\alpha=v,c}\mathcal{W}(\boldsymbol{\xi})\,c^\dagger_{\alpha,\tau,\sigma}(\mathbf{k}+\boldsymbol{\xi})c_{\alpha,\tau,\sigma}(\mathbf{k}), \tag{8b}$$

where S is the sample area. The donor ion is treated as a dispersionless scatterer, and is assumed to be present in the MoX_2 (electron) layer. Henceforth, we assume that a donor yields a single electron to the TMD and set $Z_{\text{donor}} = 1$.

The radiative recombination of electrons and holes is driven by the light-matter interaction

$$\hat{H}_{\text{r}} = \frac{e\gamma}{\hbar c}\sum_{\mathbf{q}}\sum_{\mathbf{k},\tau,\sigma}\sqrt{\frac{4\pi\hbar c}{Vq}}c^\dagger_{v,\tau,\sigma}(\mathbf{k}-\mathbf{q}_\parallel)c_{c,\tau,\sigma}(\mathbf{k})a^\dagger_\tau(\mathbf{q}) \tag{9}$$

in the WX_2 layer and an analogous term $\hat{H}'_{\text{r}}$ in the MoX_2 layer. Here, $\gamma^{(\prime)}$ is given by the in-plane momentum matrix element between $c^{(\prime)}$ and $v^{(\prime)}$ band states, evaluated at the $\pm K$ points of the BZ [32]. $a^\dagger_\tau(\mathbf{q})$ creates a photon of momentum $\mathbf{q}$ and in-plane polarization τ, determined by the electron's valley degree of freedom, where $\tau = +$ ($\tau = -$) represents right-handed (left-handed) circular polarization. The photon momentum $\mathbf{q} = \mathbf{q}_\parallel + \mathbf{q}_\perp$ is split into its in-plane and out-of-plane components, respectively, and $V = SL$, with L the height of the optical cavity in which the sample is embedded.

Let $|\Psi\rangle$ be an interlayer excitonic eigenstate of the Hamiltonian $\hat{H}_0 + \hat{U}_{\text{intra}} + \hat{U}_{\text{inter}}$ of energy E_Ψ. Photon emission through the term $\hat{H}_{\text{r}}$ requires the recombining carriers to be in the same TMD layer. This is allowed by the perturbation $\hat{H}_{\text{t}}$, giving the first-order correction to the wave function,

$$|\Psi^{(1)}\rangle = \sum_n \frac{\langle n|\hat{H}_{\text{t}}|\Psi\rangle}{E_n - E_\Psi}|n\rangle, \tag{10}$$

where the sum runs over the eigenstates $|n\rangle$ of $\hat{H}_0 + \hat{U}_{\text{intra}} + \hat{U}_{\text{inter}}$, with energies E_n. The resulting rate of radiative recombination is then given by Fermi's golden rule as

$$\Gamma_\Psi = \frac{2\pi}{\hbar}\sum_f |\langle f|[\hat{H}_{\text{r}} + \hat{H}'_{\text{r}}]|\Psi^{(1)}\rangle|^2\delta(E_f - E_\Psi), \tag{11}$$

where $\{|f\rangle\}$ is the set of possible final states, containing one additional photon. As discussed below, the relevant matrix elements in Eq. (11) can be evaluated numerically in QMC.

III. RECOMBINATION OF DONOR-BOUND INTERLAYER COMPLEXES

A. Model parameters

We now discuss the optical emission signatures of the most relevant donor-bound interlayer excitonic complexes predicted by VMC and DMC simulations. For concreteness, we will focus on $MoSe_2/WSe_2$ heterobilayers (X = Se); parameters relevant to this pair of materials are shown in Table I. Furthermore, we assume that the heterobilayer is encapsulated in bulk hBN, and set the dielectric constant to $\epsilon = 4$. Our chosen value of 4 corresponds to the high-frequency dielectric constant of hBN, which is reasonable as the exciton binding energy is considerably larger than the highest optical phonon frequency of hBN. In principle, the anisotropic nature of the encapsulating hBN supplies an effective dielectric constant $\bar{\epsilon} = \sqrt{\epsilon_\parallel\epsilon_\perp}$ and renormalizes the interlayer distance d by a factor $\sqrt{\epsilon_\parallel/\epsilon_\perp}$, where $\epsilon_\parallel$ and $\epsilon_\perp$ are the in-plane and out-of-plane dielectric

TABLE I. Model parameters for $MoSe_2$ and WSe_2, extracted from Refs. [21,23,32,37,38], and the heterobilayer $MoSe_2/WSe_2$ extracted from Refs. [10,12,39]. The interlayer gap $\tilde{E}_{\text{g}}$ was estimated from the luminescence spectrum reported in Ref. [12], considering the exciton binding energies of Table II. From left to right, the single-layer parameters are lattice constant a, VB and CB masses m_v and m_c, screening length r_* in a vacuum environment, and momentum matrix element γ. The heterobilayer parameters are valence and conduction interlayer spacing Δ_v and Δ_c, interlayer band gap $\tilde{E}_{\text{g}}$, and interlayer distance d.

	a (Å)	m_v/m_0	m_c/m_0	r_* (Å)	γ (eV Å)
$MoSe_2$	3.30	0.44	0.38	39.79	2.53
WSe_2	3.29	0.34	0.29	45.11	3.17
		Δ_v (eV)	Δ_c (eV)	$\tilde{E}_{\text{g}}$ (eV)	d (Å)
$MoSe_2/WSe_2$		0.36	0.36	1.5	6.48

TABLE II. Binding energies $\mathcal{E}^{\rm b}$ of some charge-carrier complexes in a $MoSe_2$ monolayer, a WSe_2 monolayer, and a $MoSe_2/WSe_2$ heterobilayer in different dielectric environments including vacuum on both sides, SiO_2 on one side and vacuum on the other, bulk hBN on one side and vacuum on the other, and bulk hBN on both sides. In the heterobilayer, it is assumed that the donor ion and electrons occur in the $MoSe_2$ layer, while the holes are confined in the WSe_2 layer. The material parameters are listed in Table I. The DMC error bars are everywhere smaller than 0.2 meV.

		Binding energy (meV)			
System	ϵ	$X_{vc'}$	$X^-_{vc'c'}$	$D^0_{c'}$	$D^0_{c'}X_{vc'}$
hBN/$MoSe_2$/hBN	4	194	16.2	260	21.0
hBN/WSe_2/hBN	4	160	13.6	215	18.1
vac./$MoSe_2$/WSe_2/vac.	1	206	6.2	540	40.3
SiO_2/$MoSe_2$/WSe_2/vac.	2.45	123	5.1	329	30.1
hBN/$MoSe_2$/WSe_2/vac.	2.5	121	5.2	324	29.9
hBN/$MoSe_2$/WSe_2/hBN	4	84.2	4.1	229	22.5

constants (see Appendix A). However, taking $\epsilon_\parallel(\infty)$ and $\epsilon_\perp(\infty)$ from various sources we find that $3.1 < \sqrt{\epsilon_\parallel\epsilon_\perp} < 4.5$ and $0.71 < \sqrt{\epsilon_\parallel/\epsilon_\perp} < 0.95$ [33–36]. This justifies, in part, our use of $\epsilon = 4$ and our use of the unmodified physical layer separation, but as a check of the robustness of our results, we have also considered a few other dielectric environments for a restricted set of charge complexes.

The Hamiltonian of Eq. (4), without $\hat{H}_{\rm t}$ (i.e., with charges being fixed in their layers), was solved using DMC for various numbers of excess electrons and holes, and in the presence of donor impurities in the $MoSe_2$ layer. Our DMC total energies are statistically exact: we have not considered any complexes containing indistinguishable fermions, and therefore the ground-state wave functions are nodeless, so that no fixed-node error is incurred. The technical details of our DMC calculations are given in Appendix B 1. Binding energies for free and impurity-bound excitons and trions, in different dielectric environments, are reported in Table II. DMC binding energies for a wider range of charge-carrier complexes in heterobilayers are reported in Table V in Appendix B 2. A number of donor-bound complexes with up to four electrons and two holes are predicted to be stable. A detailed account of the sensitivity of the binding energy of $D^0_{c'}X_{vc'}$ to our choices of model parameter ($m_{c'}$, m_v, r_*, r'_*, d, and ϵ) is given in Appendix B 3.

The simplest interlayer excitonic complex is a donor-bound exciton $D^0_{c'}h_v$, where $D^0_{c'}$ represents a positive donor ion that has been neutralized by binding an electron from band c', and h_v a hole from band v. (When complex labels appear as subscripts in formulas, we will suppress the v and c subscripts for clarity.) DMC simulations predict that this complex is unbound due to the screening of the interlayer interaction between holes and the strongly bound neutral donor state $D^0_{c'}$, whose binding energy is $\mathcal{E}^{\rm b}_{D^0} = -229.03$ meV (Table II). We therefore consider the recombination of a neutral donor $D^0_{c'}$ with delocalized holes in band v.

Adding one more electron we obtain a donor-bound trion. Alternatively, this complex can be viewed as an interlayer exciton $X_{vc'}$ bound by a neutral donor $D^0_{c'}$, leading to the notation $D^0_{c'}X_{vc'}$. Remarkably, this larger complex is stable up to ∼256 K, with binding energy $\mathcal{E}^{\rm b}_{D^0X} \approx 22.52$ meV (Table II) for the most energetically favorable dissociation channel into a neutral donor $D^0_{c'}$ and an interlayer exciton $X_{vc'}$. In the following sections, we calculate the photoemission rates of these two complexes using the formalism described in Sec. II.

B. $D^0_{c'}h_v$: Neutral donor and free hole

The initial state for the recombination process of a neutral donor and a free hole is given in second quantization by

$$|D^0;\mathbf{k}_{\rm h}\rangle = \frac{1}{\sqrt{S}}\sum_{\mathbf{k}} \tilde{\chi}_{\mathbf{k}}\, c^\dagger_{c',\tau',\sigma'}(\mathbf{k})c_{v,\tau,\sigma}(\mathbf{k}_{\rm h})|\Omega\rangle, \qquad (12)$$

where $\tilde{\chi}_{\mathbf{k}} = \int \chi(\mathbf{r})e^{-i\mathbf{k}\cdot\mathbf{r}}\,d^2r$ is the Fourier transform of the donor-atom wave function centered at the donor site. Relative to the neutral vacuum, the state's energy can be written as $E_{D^0}(\mathbf{k}_{\rm h}) = E_{c'}(0) - E_v(\mathbf{k}_{\rm h}) - \mathcal{E}^{\rm b}_{D^0}$, with $\mathcal{E}^{\rm b}_{D^0}$ the binding energy.

In the close-alignment limit and in the absence of intervalley scattering, the complex described by Eq. (12) can decay through radiative recombination only if $\tau' = \tau$. Furthermore, spin-valley locking [37] and the known band ordering of $MoSe_2$ and WSe_2 monolayers [32] further require that $\sigma = \sigma'$. Considering single-photon final states of the form $|f\rangle = a^\dagger_\tau(\mathbf{q})|\Omega\rangle$, with polarization determined by the valley quantum number, and assuming a small twist angle $\theta \approx 0°$, Eqs. (10) and (11) give the radiative decay rate

$$\Gamma^<_{D^0h} = \frac{4\tilde{E}_{\rm g}|F(\mathbf{r}_0)|^2}{\hbar}\frac{e^2}{\hbar c}\left[\frac{t_{vv}\gamma'}{\hbar c\Delta_v} - \frac{t_{cc}\gamma}{\hbar c\left(\Delta_c + \mathcal{E}^{\rm b}_{D^0}\right)}\right]^2 \times\left|\int d^2r\, e^{i\Delta\mathbf{K}\cdot\mathbf{r}}\chi(\mathbf{r})\right|^2 n_{\rm h}, \qquad (13)$$

where $n_{\rm h}$ is the hole density of the sample, and the stacking-dependent function $F(\mathbf{r}_0) = 1 + e^{-i\mathbf{G}_1\cdot\mathbf{r}_0} + e^{-i\mathbf{G}_2\cdot\mathbf{r}_0}$ is introduced by the momentum-conservation rule in Eq. (7) (see also Fig. 10 in Appendix C). To evaluate Eq. (13), we obtain the wave function $\chi(\mathbf{r})$ of the donor-bound electron by solving the two-body problem with a finite-elements method, as detailed in Appendix E. Note that a finite amplitude for radiative recombination depends critically on the electron-hole asymmetry, and on having different tunneling strengths between the CBs and the VBs of the two layers, owing to the symmetry properties of the band states.

C. $D^0_{c'}X_{vc'}$: Donor-bound interlayer trion

As discussed above, a donor-bound trion $D^0_{c'}X_{vc'}$ can be viewed as an interlayer exciton bound to a neutral donor ion. Defining the interlayer exciton $X_{vc'}$ and $D^0_{c'}$ energies as $E_X = E_{c'}(0) - E_v(0) - \mathcal{E}^{\rm b}_X$ and $E_{D^0} = E_{c'}(0) - \mathcal{E}^{\rm b}_{D^0}$, respectively, the energy of a $D^0_{c'}X_{vc'}$ complex can be expressed as $E_{D^0X} = E_{D^0} + E_X - \mathcal{E}^{\rm b}_{D^0X}$, where $\mathcal{E}^{\rm b}_{D^0X}$ is the binding energy defined with respect to the most favorable dissociation channel into $D^0_{c'} + X_{vc'}$. The corresponding eigenstate is given by

$$|D^0X\rangle = \frac{1}{S^{3/2}}\sum_{\mathbf{k}_{\rm h},\mathbf{k}_1,\mathbf{k}_2}\tilde{\Phi}_{\mathbf{k}_{\rm h},\mathbf{k}_1,\mathbf{k}_2} \times c^\dagger_{c',\tau',\sigma}(\mathbf{k}_1)c^\dagger_{c',-\tau',-\sigma'}(\mathbf{k}_2)c_{v,\tau,\sigma}(\mathbf{k}_{\rm h})|\Omega\rangle, \qquad (14)$$

with its two electrons belonging to opposite valleys, thus minimizing their mutual repulsion [see Eqs. (1a) and (1b)]. In this case, we consider decay into states of the form $|f\rangle = a_\tau^\dagger(\mathbf{q})|\mathrm{D}^0\rangle$, which are energetically favorable given the large binding energies of $\mathrm{D}^0_{c'}$ bound states. The corresponding radiative rate for close interlayer alignment is given by

$$\Gamma^{<}_{\mathrm{D}^0\mathrm{X}} \approx \frac{4\tilde{E}_\mathrm{g}}{\hbar}\frac{e^2}{\hbar c}|F(\mathbf{r}_0)|^2 \times\left|\int d^2r\int d^2r'\, e^{i\Delta\mathbf{K}\cdot\mathbf{r}}\chi^*(\mathbf{r}')\Phi(\mathbf{r},\mathbf{r},\mathbf{r}')\right|^2 \times\left[\frac{t_{vv}\gamma'}{\hbar c\left(\Delta_v+\mathcal{E}^\mathrm{b}_{\mathrm{D}^0\mathrm{X}}+\mathcal{E}^\mathrm{b}_X\right)}-\frac{t_{cc}\gamma}{\hbar c\left(\Delta_c+\mathcal{E}^\mathrm{b}_{\mathrm{D}^0\mathrm{X}}+\mathcal{E}^\mathrm{b}_\mathrm{X}\right)}\right]^2. \tag{15}$$

The donor atom in the final state can be in its ground state, or in any excited state allowed by angular momentum conservation. This constitutes a series of radiative subchannels, and in principle results in a series of lines with energies determined by the donor atom spectrum. The main subchannel, corresponding to the ground state $\chi_{1s}(\mathbf{r})$, produces the main emission line at $E_* = \tilde{E}_g - (\mathcal{E}^\mathrm{b}_{\mathrm{D}^0\mathrm{X}} + \mathcal{E}^\mathrm{b}_\mathrm{X})$. The first radially symmetric excited state, $\chi_{2s}(\mathbf{r})$, will produce an additional line ~167 meV above the main line. The overlap integrals between the ground-state donor-bound trion and the $1s$ and $2s$ neutral donor states were evaluated using VMC, and the latter was found to be two orders of magnitude smaller. We conclude that excited states can be neglected, and henceforth only the $1s$ subchannel will be considered. In the case of $\Delta K = 0$, the integral in Eq. (15) is given by $|\int d^2r\int d^2r'\,\chi^*(\mathbf{r}')\Phi(\mathbf{r},\mathbf{r},\mathbf{r}')|^2 = 1.47$ (see Appendix B 5 for details).

To summarize Sec. III, Fig. 1(b) shows the radiative rates of $\mathrm{D}^0_{c'}\mathrm{h}_v$ and $\mathrm{D}^0_{c'}X_{vc'}$ in an hBN/$MoSe_2$/WSe_2/hBN heterostructure, for small twist angles and using the maximum value of $|F(0)|^2 = 9$. Alternatively, we may average this function within the unit cell, leading to $\langle|F(\mathbf{r}_0)|^2\rangle \approx 3$. The large-angle asymptotic behavior of the radiative rate shown in Fig. 1(b) is discussed next.

IV. ASYMPTOTIC BEHAVIOR FOR LARGE INTERLAYER TWIST ANGLES

To estimate the quenching of radiative decay as the misalignment angle grows, we evaluate the asymptotic behavior of the radiative rate for large valley mismatch $|\Delta\mathbf{K}| \gtrsim 1/a_0^*$ from a perturbative treatment of the short-range interactions (3). In this regime, the rate of radiative decay of intralayer complexes is determined by the tail of the momentum-space wave function extending toward the opposite layer valley, and which is governed by the large-momentum portion of the interaction term (8a). Thus we formally split $\hat{U}_\mathrm{intra} = \hat{U}^<_\mathrm{intra} + \hat{U}^>_\mathrm{intra}$ and $\hat{U}_\mathrm{inter} = \hat{U}^<_\mathrm{inter} + \hat{U}^>_\mathrm{inter}$, where "large" (>) momentum corresponds to wave vectors $\gtrsim 1/a_0^*$. Let $|\Psi_0\rangle$ be an excitonic state of energy E^0_Ψ, of the Hamiltonian

$$\hat{H}_\mathrm{LR} = \hat{H}_0 + \hat{U}^<_\mathrm{intra} + \hat{U}^<_\mathrm{inter}, \tag{16}$$

containing the long-range approximation to the carrier-carrier and donor-carrier interaction. The interactions $\hat{U}^<_\mathrm{intra}$ and $\hat{U}^<_\mathrm{inter}$ are given by the expressions (8a) and (8b), respectively, with

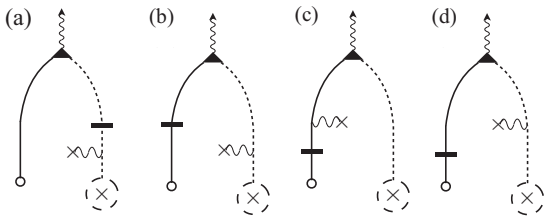

FIG. 3. Diagrams for the radiative recombination of neutral donors $\mathrm{D}^0_{c'}$ with free holes h_v. The solid (dashed) line represents a free hole (electron); the donor impurity center is represented by a "×" symbol, and the $\mathrm{D}^0_{c'}$ state by "×" in a dashed circle. Horizontal lines correspond to interlayer tunneling, wavy lines to Coulomb scattering, and the triangular vertex represents radiative recombination.

the substitutions $\mathcal{V}^{(\prime)}(\boldsymbol{\xi}) \longrightarrow \mathcal{V}^{(\prime)}_<(\boldsymbol{\xi})$ and $\mathcal{W}(\boldsymbol{\xi}) \longrightarrow \mathcal{W}_<(\boldsymbol{\xi})$ [see Eqs. (2a) and (2b)]. The state $|\Psi_0\rangle$ is perturbed by the interlayer tunneling term $\hat{H}_\mathrm{t}$, as well as the short-range interaction $\hat{U}^>_\mathrm{intra}$, obtained by substituting $\mathcal{V}^{(\prime)}(\boldsymbol{\xi}) \longrightarrow \mathcal{V}^{(\prime)}_>(\boldsymbol{\xi})$ in Eq. (8a) [see Eq. (3)]. As shown in Eq. (3), these terms are inversely proportional to the square of a large wave number, and thus may be treated perturbatively. Furthermore, the short-range interlayer term is exponentially suppressed, and can be ignored altogether. As a consequence, short-range impurity scattering can take place exclusively in the electron layer, where the impurity centers are located (see diagrams of Fig. 3).

In second-order perturbation theory, the correction to the wave function relevant for photon emission is given by

$$\left|\Psi^{(2)}_0\right\rangle = \sum_{m,n}\frac{\langle n|[\hat{H}_\mathrm{t}+\hat{U}^>_\mathrm{intra}]|m\rangle\langle m|[\hat{H}_\mathrm{t}+\hat{U}^>_\mathrm{intra}]|\Psi_0\rangle}{\left(E^0_m-E^0_\Psi\right)\left(E^0_n-E^0_\Psi\right)}|n\rangle, \tag{17}$$

where the sums run over the eigenstates $|n\rangle$ of $\hat{H}_\mathrm{LR}$, with energies E^0_n. Introducing the light-matter interaction [Eq. (9)], we focus on the diagrams of Fig. 3 for the $\mathrm{D}^0_{c'}\mathrm{h}_v$ complex, and those of Fig. 4 for $\mathrm{D}^0_{c'}X_{vc'}$.

In general, all diagrams must be considered when evaluating the radiative decay rate. For simplicity, however, we assume that the CB and VB spacings remain the largest scales in the problem, such that $\frac{\hbar^2\Delta K^2}{2m_\alpha} \ll \Delta_c, \Delta_v$. In this approximation, two out of the four diagrams for $\mathrm{D}^0_{c'}\mathrm{h}_v$ radiative decay cancel out approximately, leaving only the contributions from the diagrams of Figs. 3(a) and 3(b) (see Appendix C). The resulting radiative decay rate for $\mathrm{D}^0_{c'}\mathrm{h}_v$ in the large twist angle (>)

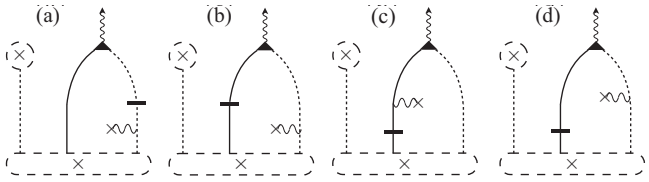

FIG. 4. Diagrams for the first radiative recombination channel of the $\mathrm{D}^0_{c'}X_{vc'}$ complex. The bound hole recombines with the electron from the nearest valley in the opposite layer, assisted by short-range Coulomb interactions with the donor impurity. The remaining electron stays bound to the impurity center, forming a neutral donor atom.

limit is

$$\Gamma^{>}_{\mathrm{D^0h}} \approx \frac{64\pi^2 e^4 \tilde{E}_\mathrm{g}}{\hbar\epsilon^2 r_*'^2 \Delta K^4}\frac{e^2}{\hbar c}\left[\frac{m_{c'}}{\hbar^2\Delta K^2}\right]^2\left[\frac{t_{cc}\gamma}{\hbar c\Delta_c}-\frac{t_{vv}\gamma'}{\hbar c\Delta_v}\right]^2 \times|\chi_0(0)|^2|F(\mathbf{r}_0)|^2 n_\mathrm{h}, \quad (18)$$

where the emitted photon energy is given by $E_* = \tilde{E}_\mathrm{g} - \mathcal{E}^\mathrm{b}_{\mathrm{D^0}}$. Finally, $\chi_0(\mathbf{r})$ is the $\mathrm{D}^0_{c'}$ wave function obtained from the Keldysh approximation Hamiltonian $\hat{H}_\mathrm{LR}$, not to be confused with the full bilayer interaction bound state $\chi(\mathbf{r})$. As before, we evaluate the wave function using the finite-element method, and obtain $|\chi_0(0)|^2 = 2.678\times10^{-3}\,\text{Å}^{-2}$ (Appendix E). We point out that evaluating the wave function $\chi_0(\mathbf{r})$ with the Keldysh potential ignores the formal wave vector cutoff that defines Eq. (16). That is, this solution considers short-range interactions within the Keldysh approximation, which, as discussed in Sec. II A, overestimate the screening length. Nonetheless, this approximation mainly affects the fast oscillating (large momentum) part of the wave function, whereas Eq. (18), and Eqs. (19) and (20) below, only depend on the smooth, small momentum part. The error incurred by this approximation is proportional to the perturbation squared, and thus beyond our first-order approximation.

With the perturbation $\hat{U}^{>}_\mathrm{intra}$, there are two possible channels for radiative recombination of the $\mathrm{D}^0_{c'}\mathrm{X}_{vc'}$ complex, resulting in different final states, and thus two separate lines in the PL spectrum. The first process involves one of the electrons and the hole scattering from the donor impurity and subsequently recombining, emitting a photon and leaving behind a neutral donor as the final state. This is analogous to the decay process considered in Sec. III C, and the corresponding diagrams are shown in Fig. 4. Similarly to the $\mathrm{D}^0_{c'}\mathrm{h}_v$ complex case, the leading approximation to the amplitude is the sum of two diagrams, giving a radiative rate

$$\Gamma^{>}_{\mathrm{D^0X}} \approx \frac{64\pi^2 e^4 \tilde{E}_\mathrm{g}}{\hbar\epsilon^2 r_*'^2 \Delta K^4}\frac{e^2}{\hbar c}\left[\frac{m_{c'}}{\hbar^2\Delta K^2}\right]^2\left[\frac{t_{cc}\gamma}{\hbar c\Delta_c}-\frac{t_{vv}\gamma'}{\hbar c\Delta_v}\right]^2 \times\left|\int d^2r\,\chi_0^*(\mathbf{r})\Phi_0(0,0,\mathbf{r})\right|^2|F(\mathbf{r}_0)|^2, \quad (19)$$

where the emitted photon energy is given by $E_* = \tilde{E}_\mathrm{g} - (\mathcal{E}^\mathrm{b}_{\mathrm{D^0X}} + \mathcal{E}^\mathrm{b}_X)$, and $\Phi_0(\mathbf{r}_\mathrm{h},\mathbf{r}_\mathrm{e},\mathbf{r}_{\mathrm{e}'})$ is the $\mathrm{D}^0_{c'}X_{vc'}$ wave function in the Keldysh approximation.

A second radiative decay process is possible, where the recombining electron and hole scatter with the second electron, at the far valley. The latter electron recoils and is unbound from the impurity, taking some amount of kinetic energy and producing a shift in the emission line. The corresponding diagrams are shown in Fig. 5 and give a recombination rate

$$\Gamma'^{>}_{\mathrm{D^0X}} = \frac{48\pi^2 e^4 \tilde{E}_\mathrm{g}}{\hbar\epsilon^2 r_*'^2 \Delta K^4}\frac{e^2}{\hbar c}\left[\frac{m_{c'}}{\hbar^2\Delta K^2}\right]^2\left[\frac{t_{cc}\gamma}{\hbar c\Delta_c}-\frac{t_{vv}\gamma'}{\hbar c\Delta_v}\right]^2 \times\int d^2r\,|\Phi_0(\mathbf{r},\mathbf{r},\mathbf{r})|^2. \quad (20)$$

The photon energy in this case is given by $E_* = \tilde{E}_\mathrm{g} - \mathcal{E}^\mathrm{b}_{\mathrm{D^0}} - \mathcal{E}^\mathrm{b}_{\mathrm{D^0X}} - \mathcal{E}^\mathrm{b}_X - \frac{\hbar^2\Delta K^2}{2m_{c'}}$, and the corresponding line in the PL spectrum is redshifted with respect to that of the first channel by ∼100 meV. Notice the absence of the interference term $|F(\mathbf{r}_0)|^2$. For this decay channel, the three tunneling processes encoded in Eq. (7) result in different momenta for the recoiling electron, and consequently in three distinguishable final states that cannot interfere.

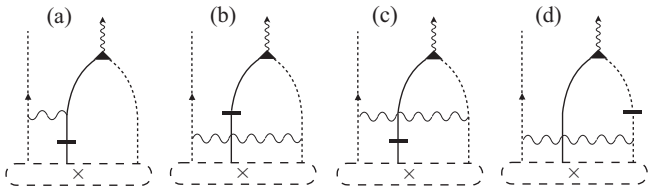

FIG. 5. Diagrams for the second radiative recombination channel of the $\mathrm{D}^0_{c'}X_{vc'}$ complex. The bound hole recombines with the electron from the nearest valley in the opposite layer, assisted by short-range Coulomb interactions with the second electron, at the far valley. The latter recoils and unbinds from the donor impurity.

The overlap integrals between the initial- and final-state wave functions given in Eqs. (19) and (20) were evaluated in VMC for the Hamiltonian $\hat{H}_\mathrm{LR}$. We obtain $|\int d^2r\,\chi_0^*(\mathbf{r})\Phi_0(0,0,\mathbf{r})|^2 = 6.94\times10^{-7}\,\text{Å}^{-4}$, and $\int d^2r\,|\Phi_0(\mathbf{r},\mathbf{r},\mathbf{r})|^2 = 3.22\times10^{-7}\,\text{Å}^{-4}$, respectively (see Appendix B 5).

Equations (18)–(20) show that the radiative channels considered for the two complexes decay with the interlayer twist angle as θ^{-8}, in the limit $\Delta K \gg 1/r_*, 1/r_*'$. This is shown in Fig. 1(b) for angles larger than 6°. Our analysis indicates that, even in the case of localized impurity-bound states, the observation of photoluminescence from interlayer excitonic complexes in TMD bilayers requires near perfect alignment between the two layers.

V. PHONON-ASSISTED RECOMBINATION

Electron-phonon (e-ph) interactions introduce yet another channel for radiative recombination. Similarly to the electron recoil process discussed above, when phonons are emitted during the recombination of a given complex, they absorb part of the energy and produce a red-shifted replica in the PL spectrum. The following analysis is carried out in terms of the VMC wave functions $|\Psi\rangle$ discussed in Sec. III, evaluated with the exact bilayer interactions $\mathcal{V}^{(\prime)}(\boldsymbol{\xi})$ and $\mathcal{W}(\boldsymbol{\xi})$.

The e-ph interaction Hamiltonian is given by

$$\hat{H}_\text{e-ph} = \sum_{\alpha=v,c}\sum_{\tau,\sigma}\sum_{\mathbf{k},\mathbf{q},\nu}\frac{g_{\nu,\alpha}(\mathbf{q})}{\sqrt{S}}(b^\dagger_{h,\nu,-\mathbf{q}} + b_{h,\nu,\mathbf{q}}) \times c^\dagger_{\alpha,\tau,\sigma}(\mathbf{k}+\mathbf{q})c_{\alpha,\tau,\sigma}(\mathbf{k}) + \sum_{\alpha=v',c'}\sum_{\tau,\sigma}\sum_{\mathbf{k},\mathbf{q},\nu}\frac{g_{\nu,\alpha}(\mathbf{q})}{\sqrt{S}}(b^\dagger_{e,\nu,-\mathbf{q}} + b_{e,\nu,\mathbf{q}}) \times c^\dagger_{\alpha,\tau,\sigma}(\mathbf{k}+\mathbf{q})c_{\alpha,\tau,\sigma}(\mathbf{k}), \quad (21)$$

where $b^\dagger_{\Lambda,\nu,\mathbf{q}}$ ($b_{\Lambda,\nu,\mathbf{q}}$) is the creation (annihilation) operator for a phonon of momentum $\mathbf{q}$ and mode ν in the electron ($\Lambda = \mathrm{e}$) or hole ($\Lambda = \mathrm{h}$) layer, which couples to an electron in band $\alpha = c', v', c, v$ with strength $g_{\nu,\alpha}(\mathbf{q})$.

We consider the longitudinal optical ($\nu = \mathrm{LO}$), homopolar ($\nu = \mathrm{HP}$), and longitudinal acoustic ($\nu = \mathrm{LA}$) phonon modes allowed by the lattice symmetry. The e-ph couplings are given by

$$\begin{aligned} g_{\mathrm{LO},\alpha}(\mathbf{q}) &= \frac{1}{A}\sqrt{\frac{\hbar}{2\rho(M_\mathrm{r}/M)\omega_\mathrm{LO}}}\frac{2\pi Z_\alpha e^2}{1+qr_*}, \\ g_{\mathrm{HP},\alpha}(\mathbf{q}) &= \sqrt{\frac{\hbar}{2\rho\omega_\mathrm{HP}}}D_\alpha, \\ g_{\mathrm{LA},\alpha}(\mathbf{q}) &= \sqrt{\frac{\hbar}{2\rho\omega_\mathrm{LA}}}\Xi_\alpha\, q, \end{aligned} \tag{22}$$

where ρ is the mass density, M_r is the metal-and-two-chalcogen system reduced mass, M is the total mass of the unit cell, and A is the unit-cell area of the corresponding TMD layer. ω_ν is the phonon frequency, which we approximate as a constant for the optical modes, and as $\omega_\mathrm{LA} = c_\mathrm{LA}\, q$ for the LA mode, with c_LA being the sound velocity. Z is the Born effective charge, r_* is the screening length, and D_α and Ξ_α are the deformation potentials of the optical and acoustic modes, respectively. The various parameters are taken from Refs. [40–43], and summarized in Table III. We focus on the low-temperature limit, where phonon occupation is low and phonon absorption can be neglected.

Perturbative corrections to the interlayer excitonic state $|\Psi\rangle$ by the interlayer hopping and e-ph interactions are given by

$$|\Psi^{(2)}\rangle = \sum_{m,n}\frac{\langle n|[\hat{H}_\mathrm{t}+\hat{H}_\text{e-ph}]|m\rangle\langle m|[\hat{H}_\mathrm{t}+\hat{H}_\text{e-ph}]|\Psi\rangle}{(E_m-E_\Psi)(E_n-E_\Psi)}|n\rangle. \tag{23}$$

The relevant diagrams for radiative recombination with phonon emission are shown in Figs. 6 and 7 for $\mathrm{D}^0_{c'}\mathrm{h}_v$ and $\mathrm{D}^0_{c'}X_{vc'}$, respectively. In both figures, panels (a)–(d) correspond to single-phonon emission in the hole layer (WSe_2), whereas panels (e)–(h) correspond to single-phonon emission in the electron layer ($MoSe_2$). Although, in principle, the two sets of diagrams give separate lines at energies determined by the phonon energy in each layer, the parameters reported in Table V show that these lines are within only a few meV of each other. For simplicity, we assume that the two layers have the same optical-phonon energies and the same acoustic-phonon sound velocities, producing a single line in the PL spectrum. The resulting radiative rates are given in the limit of large twist angle ($>$) by (Appendix D)

$$\Gamma^{>,\nu}_{\mathrm{D^0h}} \approx \frac{48\tilde{E}_\mathrm{g}}{\hbar}\frac{e^2}{\hbar c}\left[\frac{\gamma' t_{vv}}{\hbar c\Delta_v}-\frac{\gamma t_{cc}}{\hbar c\Delta_c}\right]^2 n_\mathrm{h}\left[\left(\frac{m_v g_{v,v}(\Delta K)}{\hbar^2\Delta K^2}\right)^2+\left(\frac{m_{c'}g_{v,c'}(\Delta K)}{\hbar^2\Delta K^2}\right)^2\right], \tag{24a}$$

$$\Gamma^{>,\nu}_{\mathrm{D^0X}} \approx \frac{48\tilde{E}_\mathrm{g}}{\hbar}\frac{e^2}{\hbar c}\left[\frac{\gamma' t_{vv}}{\hbar c\Delta_v}-\frac{\gamma t_{cc}}{\hbar c\Delta_c}\right]^2\left[\left(\frac{m_v g_{v,v}(\Delta K)}{\hbar^2\Delta K^2}\right)^2+\left(\frac{m_{c'}g_{v,c'}(\Delta K)}{\hbar^2\Delta K^2}\right)^2\right]\int d^2r\left|\int d^2r'\,\chi^*(\mathbf{r}')\Phi(\mathbf{r},\mathbf{r},\mathbf{r}')\right|^2. \tag{24b}$$

The VMC estimate of the overlap of $\chi(\mathbf{r}')$ with $\Phi(\mathbf{r},\mathbf{r},\mathbf{r}')$ is 3.85×10^{-4} Å^{-2}; see Table VII.

In the small-twist-angle limit ($<$), phonon emission from $\mathrm{D}^0_{c'}\mathrm{h}_v$ complexes is dominated by the diagram of Fig. 6(a). In that process, the phonon is emitted by a hole in the WSe_2 layer, which then tunnels to recombine with the electron bound to the donor impurity. By contrast, all other diagrams shown in Fig. 6 involve ionization of the donor atom, which is suppressed by the large binding energy of the $\mathrm{D}^0_{c'}$ complex. The radiative rates for $\mathrm{D}^0_{c'}\mathrm{h}_v$ can thus be approximated by (Appendix D)

$$\Gamma^{<,\nu=\mathrm{LO/HP}}_{\mathrm{D^0h}} \approx \frac{2\tilde{E}_\mathrm{g}}{\pi\hbar}\frac{e^2}{\hbar c}\left[\frac{\gamma' t_{vv}}{\hbar c\Delta_v}\right]^2\left[\frac{3|g_{v,c'}(\Delta K)|^2}{\left(\hbar\omega_v+\mathcal{E}^\mathrm{b}_{\mathrm{D^0}}\right)^2}+\frac{m_v|g_{v,v}(\Delta K)|^2|F(\mathbf{r}_0)|^2}{\hbar^3\omega_v}\left|\int d^2r\, e^{i\Delta\mathbf{K}\cdot\mathbf{r}}\chi(\mathbf{r})\right|^2\right]n_\mathrm{h}, \tag{25a}$$

$$\Gamma^{<,\mathrm{LA}}_{\mathrm{D^0h}} \approx \frac{2\tilde{E}_\mathrm{g}}{\pi\hbar}\frac{e^2}{\hbar c}\frac{m_v\,\Xi_v^2}{\hbar^2\rho c_\mathrm{LA}^2}\left[\frac{\gamma' t_{vv}}{\hbar c\Delta_v}\right]^2\left|\int d^2r\, e^{i\Delta\mathbf{K}\cdot\mathbf{r}}\chi(\mathbf{r})\right|^2|F(\mathbf{r}_0)|^2 n_\mathrm{h}. \tag{25b}$$

In the $\mathrm{D}^0_{c'}X_{vc'}$ case at small twist angles, the phonon emission process is suppressed by the ionization of the complex in the intermediate state and the overlap integral between the initial $\mathrm{D}^0_{c'}X_{vc'}$ and final $\mathrm{D}^0_{c'}$ states. The rates are given by

$$\Gamma^{<,\nu=\mathrm{LO/HP}}_{\mathrm{D^0X}} = \frac{4\tilde{E}_\mathrm{g}}{\hbar}\frac{e^2}{\hbar c}\frac{|F(\mathbf{r}_0)|^2|g_{v,v}(0)|^2+3|g_{v,c'}(0)|^2}{\left(\hbar\omega_v+\mathcal{E}^\mathrm{b}_{\mathrm{D^0X}}+\mathcal{E}^\mathrm{b}_X\right)^2}\left[\frac{\gamma' t_{vv}}{\hbar c\Delta_v}-\frac{\gamma t_{cc}}{\hbar c\Delta_c}\right]^2\int d^2r\left|\int d^2r'\,\chi^*(\mathbf{r}')\Phi(\mathbf{r},\mathbf{r},\mathbf{r}')\right|^2, \tag{26a}$$

$$\begin{aligned}\Gamma^{<,\mathrm{LA}}_{\mathrm{D^0X}} = \frac{\tilde{E}_\mathrm{g}}{\sqrt{2}\hbar^3 c_\mathrm{LA}}\frac{e^2}{\hbar c}\frac{(m_v+m_{c'})^{3/2}}{\sqrt{\mathcal{E}^\mathrm{b}_{\mathrm{D^0X}}+\mathcal{E}^\mathrm{b}_X}}\left[\frac{\gamma' t_{vv}}{\hbar c\Delta_v}-\frac{\gamma t_{cc}}{\hbar c\Delta_c}\right]^2\left[\frac{|F(\mathbf{r}_0)|^2\Xi_v^2}{\rho}\left|\int d^2r\int d^2r'\,\mathrm{e}^{-i\Delta\mathbf{K}\cdot\mathbf{r}}\chi^*(\mathbf{r}')\Phi(\mathbf{r},\mathbf{r},\mathbf{r}')\right|^2\right.\\ \left.+\frac{3\Xi_{c'}^2}{\rho'}\left|\int d^2r\int d^2r'\,\mathrm{e}^{i\Delta\mathbf{K}\cdot\mathbf{r}}\,\chi^*(\mathbf{r}')\Phi(\mathbf{r},\mathbf{r},\mathbf{r}')\right|^2\right],\end{aligned} \tag{26b}$$

TABLE III. Electron-phonon coupling parameters for LO, HP, and LA phonon modes. ω_{LO} and ω_{HP} are the LO- and HP-mode frequencies, c_{LA} is the speed of sound for the LA mode, ρ is the mass density, D_α and Ξ_α are the deformation potentials of the optical and acoustic modes, respectively, M_{r}/M is the ratio of the metal-and-two-chalcogen system reduced mass to the total mass of the unit cell, and Z is the Born effective charge.

	$\hbar\omega_{\mathrm{LO}}$ (meV)	$\hbar\omega_{\mathrm{HP}}$ (meV)	c_{LA} (cm/s)	ρ (g/cm^2)	D_c (eV/Å)	D_v (eV/Å)	Ξ_c (eV)	Ξ_v (eV)	M_{r}/M	Z
$MoSe_2$	37	30	4.8×10^5	4.5×10^{-7}	5.2	4.9	3.4	2.8	0.235	1.8
WSe_2	31	31	4.4×10^5	6.1×10^{-7}	2.3	3.1	3.2	2.1	0.249	1.08

where ρ and ρ' are the mass densities of WSe_2 and $MoSe_2$, respectively (Table V).

In Eqs. (24a)–(26b), the electron-layer contributions to the decay rate contain a factor of three originating from the tunneling process, which gives three distinct intermediate states with different emitted phonon wave vectors, related by C_3 symmetry. As a result, the interference factor appearing in the interaction-driven processes of Secs. III and IV is absent in this case. For the hole layer, however, the interference factor remains due to the momentum spread of the complex wave function, which lifts the requirement that the hole be scattered exactly onto the electron-layer valley in order to recombine.

Additional contributions to the LO phonon emission come from e-ph interaction of a carrier in one layer with an LO phonon in the other. This is made possible by the long range of the LO phonon-induced potential. The interlayer separation results in an exponential suppression of the potential in the interlayer distance and momentum transfer as $e^{-\Delta K d}$, which nonetheless is approximately unity in the limit of close alignment. Thus we add this contribution to the LO-phonon-assisted recombination rates for $\mathrm{D}^0_{c'}\mathrm{h}_v$ and $\mathrm{D}^0_{c'}X_{vc'}$ complexes in the small-twist-angle limit.

The total phonon emission rates for the two complexes, combining the three phonon modes, are shown in Fig. 1(b) as functions of the twist angle. As mentioned above, the phonon contribution to the recombination rate is most significant for the $\mathrm{D}^0_{c'}\mathrm{h}_v$ complex, being an order of magnitude larger than for $\mathrm{D}^0_{c'}X_{vc'}$. The LO phonon mode in the hole layer (WSe_2) is the dominant phonon-assisted process overall, and gives a significant decay rate in the small-twist-angle limit. As a result, we predict additional phonon-replica lines in the PL spectrum, redshifted by the phonon energy $\hbar\omega_{\mathrm{LO}} = 31$ meV with respect to the main $\mathrm{D}^0_{c'}\mathrm{h}_v$ and $\mathrm{D}^0_{c'}X_{vc'}$ lines. The $\mathrm{D}^0_{c'}\mathrm{h}_v$ phonon-replica line gives the most dominant feature, with decay rates comparable to the main $\mathrm{D}^0_{c'}\mathrm{h}_v$ line.

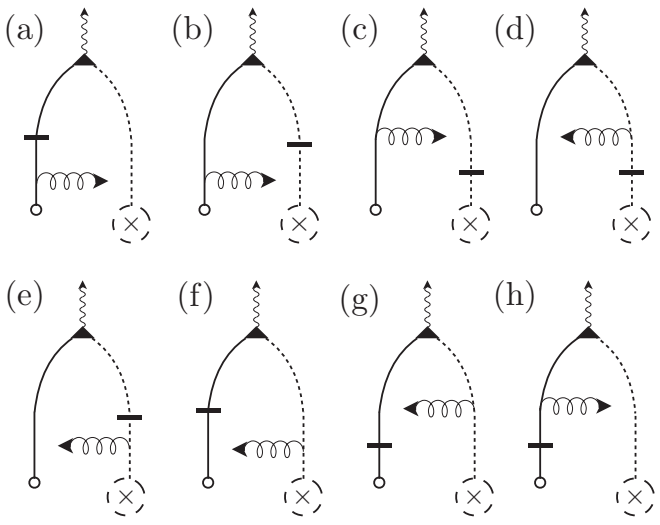

FIG. 6. Diagrams for the radiative recombination of the $\mathrm{D}^0_{c'}\mathrm{h}_v$ complex with phonon scattering. The top four diagrams correspond to phonon emission in the WSe_2 layer and the bottom four diagrams correspond to phonon emission in the $MoSe_2$ layer.

VI. INTENSITY DEPENDENCE ON DOPING

In addition to the decay rates, the relative line intensities also depend on the distribution of $\mathrm{D}^0_{c'}\mathrm{h}$ and $\mathrm{D}^0_{c'}\mathrm{X}_{vc'}$ complexes in the system. At charge neutrality, neutral excitonic complexes such as $\mathrm{D}^0_{c'}\mathrm{h}_v$ are energetically favorable, whereas additional electrons introduced into the sample will bind to existing neutral donors to form $\mathrm{D}^0_{c'}\mathrm{X}_{vc'}$ complexes. Thus the relative population of complexes can be controlled through doping.

In this section, we model the evolution of the PL spectrum with the electron carrier density within the range $0 < n_{\mathrm{e}} \leqslant 2n_{\mathrm{D}}$, controlled by means of gating [18]. We use a simplified zero-temperature model for the occupations of the two complexes, shown in Fig. 8. There are two main regimes determined by the sample-dependent donor density n_{D}. In the p-doped regime, defined by $0 < n_{\mathrm{e}} < n_{\mathrm{D}}$, added electrons neutralize the excess positive donors, forming $\mathrm{D}^0_{c'}$ complexes that can recombine with the optically pumped holes. In this regime, the formation of $\mathrm{D}^0_{c'}\mathrm{X}_{vc'}$ complexes is energetically unfavorable, and thus thermally suppressed until all donors have been neutralized. By contrast, in the n-doped regime, defined by $n_{\mathrm{D}} < n_{\mathrm{e}} < 2n_{\mathrm{D}}$, it is energetically favorable for additional electrons to bind with an existing neutral donor

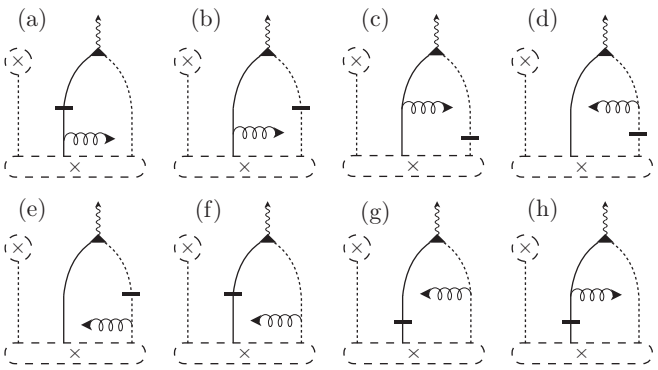

FIG. 7. Diagrams for the radiative recombination of the $\mathrm{D}^0_{c'}X_{vc'}$ complex with phonon scattering and $\mathrm{D}^0_{c'}$ in the final state. The top four diagrams correspond to phonon emission in the WSe_2 layer and the bottom four diagrams correspond to phonon emission in the $MoSe_2$ layer.

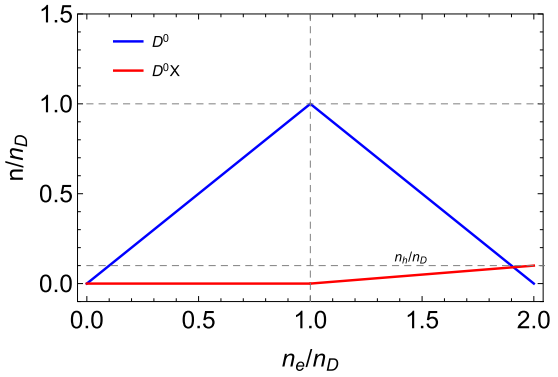

FIG. 8. Model for the density of complexes $D^0_{c'}$ and $D^0_{c'}X_{vc'}$ as a function of the electron density n_e.

to form either a charged donor state $D^-_{c'c'}$ (Table IV), or a donor-bound trion $D^0_{c'}X_{vc'}$. For the latter case we must consider that laser-pumped holes are scarce ($n_h \ll n_D$), and thus the probability of forming a $D^0_{c'}X_{vc'}$ complex will be proportional to n_h/n_D. The increase in electron density is accompanied by a decrease in $D^0_{c'}h_{v'}$ numbers, and a much slower increase in the $D^0_{c'}X_{vc'}$ population, until the number of donor-bound trions in the system equals the number of available holes. This is shown in Fig. 8, and can be summarized as

$$n_{D^0} = \begin{cases} n_e, & n_e < n_D \\ n_D\left[1 - \frac{n_e - n_D}{n_D}\right], & n_D < n_e < 2n_D \end{cases} \tag{27}$$

and

$$n_{D^0X} = \begin{cases} 0, & n_e < n_D \\ n_D \frac{n_h}{n_D} \frac{n_e - n_D}{n_D}, & n_D < n_e < 2n_D \end{cases}. \tag{28}$$

Equations (27) and (28), together with (13), show the dependence of n_{D^0} and n_{D^0X} on the hole density. This dependence is critical for radiative recombination, given the scarcity of holes by comparison to the donor density. Thus, to give a realistic estimate of the intensity, we consider the effects of nonradiative recombination of holes through impurity-driven processes. The density of holes lost through these processes per unit time can be written as $\tau_0^{-1} n_h$, where τ_0^{-1} is the nonradiative decay rate. Assuming that holes are laser-pumped at a constant rate $\tau_{\text{pump}}^{-1} n_0$, where n_0 is a constant with dimensions of inverse area, the hole density obeys the rate equation

$$\dot{n}_h = \tau_{\text{pump}}^{-1} n_0 - \tau_0^{-1} n_h, \tag{29}$$

with the steady state solution $n_h = \tau_0 \tau_{\text{pump}}^{-1} n_0$. In the p-doped regime, delocalized holes can recombine nonradiatively with the electrons present in the sample, and the nonradiative lifetime can be assumed of the form $\tau_0 = c_0/n_e$, with c_0 a constant. Thus, writing the $D^0_{c'}h_v$ radiative intensity as $I_{D^0h} = \Gamma_{D^0h} n_{D^0}$, we obtain the expression

$$I_{D^0h} = \frac{4\tilde{E}_g |F(\mathbf{r}_0)|^2}{\hbar} \frac{e^2}{\hbar c} \left[\frac{t_{vv}\gamma'}{\hbar c \Delta_v} - \frac{t_{cc}\gamma}{\hbar c\left(\Delta_c + \mathcal{E}^b_{D^0}\right)} \right]^2 \times \left| \int d^2r\, e^{i\Delta\mathbf{K}\cdot\mathbf{r}} \chi(\mathbf{r}) \right|^2 c_1, \tag{30}$$

TABLE IV. DMC total energies of various charge-carrier complexes in the hBN/$MoSe_2$/WSe_2/hBN heterostructure calculated using the monolayer Keldysh approximation to the bilayer potential [Eqs. (A12) and (A15)] and using the full bilayer interaction [Eqs. (1a)–(1c)]. Primes ($'$) indicate that a charge carrier is in the $MoSe_2$ layer; otherwise, the charge carrier is in the WSe_2 layer. The subscripts c and v indicate whether charge carriers are electrons (c) or holes (v). Donor ions are always assumed to be in the $MoSe_2$ layer, while acceptor ions are always assumed to be in the WSe_2 layer. Interlayer complexes in which all the electrons are in the $MoSe_2$ layer and all the holes are in the WSe_2 layer are listed in the upper section of the table; complexes in which some of the electrons are in the WSe_2 layer are listed in the lower section of the table.

	DMC total energy (meV)	
Complex	Approx. Keldysh	Bilayer potential
$X_{vc'}$	−103.958669(5)	−84.232(1)
$X^-_{vc'c'}$	−108.1967(4)	−88.32(3)
$X^+_{vvc'}$		−88.12(2)
$X_{vc'}X_{vc'}$		unbound
$X_{vc'}X^-_{vc'c'}$		unbound
$D^0_{c'}$	−163.2478711(5)	−229.03306(1)
$D^-_{c'c'}$	−176.9426(3)	−249.60(2)
$D^0_{c'}h_v$	−163.4819(8)	unbound
$D^0_{c'}X_{vc'}$	−278.73(2)	−335.781(4)
$D^0_{c'}X^+_{vvc'}$		−340.891(6)
$D^-_{c'c'}X_{vc'}$	−292.83(1)	−343.26(3)
$D^0_{c'}X_{vc'}X_{vc'}$		unbound
$D^-_{c'c'}X_{vc'}X_{vc'}$		−430.9(1)
A^0_v		−205.24083(1)
A^+_{vv}		−223.56(1)
$A^0_v e_{c'}$		unbound
$A^0_v X_{vc'}$		−309.411(4)
$A^0_v X^-_{vc'c'}$		−315.021(8)
X_{vc}	−114.601814(1)	−140.4303329(4)
D^0_c	−124.890219(9)	−102.5996(7)
$X^-_{vcc'}$	−120.6018(5)	unbound
X^-_{vcc}	−123.7189(5)	−152.25(1)
$D^-_{cc'}$	−165.8499(5)	unbound
D^-_{cc}	−129.3199(9)	unbound
D^+X_{vc}	−133.758(2)	−141.716(8)
$D^0_{c'}X_{vc}$	−279.776(5)	unbound
$D^-_{c'c'}X_{vc}$	−301.81(1)	unbound
$D^0_{c'}X^-_{vcc}$	−295.00(1)	unbound

where $c_1 = c_0 n_0 \tau_{\text{pump}}^{-1}$ is a constant independent of the electron density.

A similar argument can be made for the n-doped regime. In this case, the intensity is given by $I_{D^0X} = \Gamma_{D^0X} n_{D^0X}$, where the number of donor-bound trions can be approximated as $n_{D^0X} = n_h(n_e - n_D)/n_D$. However, in this regime, the holes will be localized near the donor-impurity sites forming $D^0_{c'}X_{vc'}$ states, where they will be in close proximity to two electrons with which they can recombine nonradiatively. Thus we may approximate the nonradiative decay rate as $\tau_0 = c_0/2n_D$. This leads to

$$I_{D^0X} = \frac{(n_e - n_D)}{2n_D^2} c_1 \Gamma_{D^0X}. \tag{31}$$

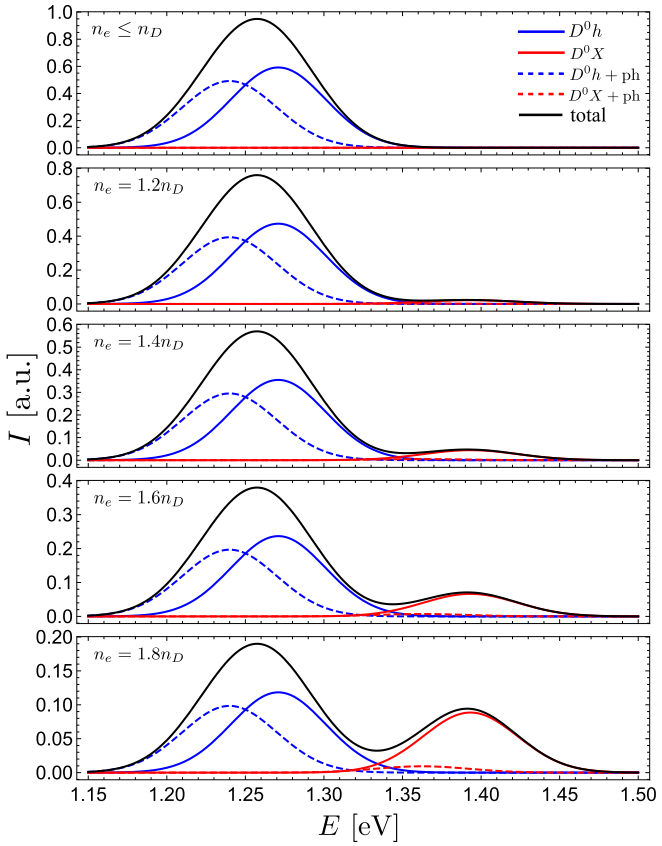

FIG. 9. Simulated normalized PL spectra for a closely aligned ($\theta \approx 0^\circ$) $MoSe_2/WSe_2$ heterobilayer, originating from the $D^0_{c'}h_v$ and $D^0_{c'}X_{vc'}$ complexes at different electron densities n_e, given in terms of the fixed donor density n_D. Dashed curves correspond to the phonon replicas. The lines are assumed to have Gaussian shapes of width $2\sigma = 60$ meV, and we use $n_h = 10^{11}$ cm^{-2} and $n_D = 10^{13}$ cm^{-2}.

The resulting simulated PL spectrum is shown in Fig. 9 for different doping densities, given in terms of the donor density in the $MoSe_2$ layer. A Gaussian line shape was used for the lines with an experimentally motivated broadening [18] of $2\sigma = 60$ meV. The spectrum shows the three dominant lines, $D^0_{c'}h_v$, $D^0_{c'}X_{vc'}$, and the redshifted phonon replica of $D^0_{c'}h_v$, with the lines' peak energies determined by the DMC-obtained binding energies. The three complexes evolve with doping as prescribed by Eqs. (30) and (31). The $D^0_{c'}h_v$ complex and its phonon replica dominate for $0 < n_e < n_D$; then, the $D^0_{c'}X_{vc'}$ line grows slowly in intensity in the n-doped regime, with a simultaneous reduction in the intensity of the $D^0_{c'}h_v$ complex. For the broadening used in the simulated PL spectrum, the proximity of the three lines results in an intricate line form, providing a signature in PL experiments for the intrinsic structure of the interlayer emission line.

VII. CONCLUSIONS

The momentum mismatch between twisted and incommensurate heterobilayer TMDs prevents efficient radiative recombination of interlayer complexes composed of electrons and holes localized on opposite layers. In this paper we described mechanisms that bridge the momentum gap involving donor impurities present in the heterobilayer system, both at small and large twist angles. The donor impurities were found to provide deep potential wells (∼200 meV), resulting in strongly bound interlayer complexes, as revealed by DMC calculations. Focusing on the simplest multiparticle complexes, we estimate radiative rates of up to a few μs^{-1} for the neutral donor with a free hole $D^0_{c'}h_v$ and the donor-bound trion $D^0_{c'}X_{vc'}$ complexes for closely aligned layers, and a strong twist-angle suppression for large misalignment with the asymptotic form $\propto\theta^{-8}$. A comparable contribution was found for the $D^0_{c'}h_v$ complex from emission of optical phonons, resulting in a total of three dominant and doping-tunable lines in the PL spectrum. The $D^0_{c'}h_v$ line and its phonon replica are expected to dominate the emission spectrum for electron densities below the sample-dependent donor concentration; conversely, PL from the $D^0_{c'}X_{vc'}$ complex is expected to dominate the interlayer sector of the spectrum when the electron density exceeds the density of donors.

Based on QMC simulations, we have shown that our qualitative results are robust against uncertainty in model parameters, such as the band effective masses, as well as sample-dependent dielectric properties. Therefore our predictions provide a new perspective for interpreting recent experimental observations of interlayer luminescence in heterobilayers of transition-metal dichalcogenides.

All relevant data present in this publication can be accessed at Lancaster University [44].

ACKNOWLEDGMENTS

M.D., D.A.R.-T., and V.I.F. wish to thank F. Vialla and F. Koppens for fruitful discussions. M.D., D.A.R.-T., and V.I.F. acknowledge support from ERC Synergy Grant Hetero2D, EPSRC EP/N010345, EPSRC EP/P026850/1, Lloyd Register Foundation Nanotechnology grant, and support from the European Graphene Flagship Project. R.J.H. is fully funded by the Graphene NOWNANO center for doctoral training (EPSRC grant no. EP/L01548X/1). M.S. was funded by the EPSRC standard grant "Non-perturbative and stochastic approaches to many-body localization" (Grant No. EP/P010180/1). Computer time was provided by Lancaster University's High-End Computing facility. This work made use of the facilities of N8 HPC Centre of Excellence, provided and funded by the N8 consortium and EPSRC (Grant No. EP/K000225/1). The Centre is coordinated by the Universities of Leeds and Manchester.

APPENDIX A: LONG-RANGE INTERACTION BETWEEN CHARGE CARRIERS

1. Multilayer Keldysh interaction

Consider a vdW heterostructure of 2D semiconductors comprised of N parallel layers (labelled $i = 1,2,\ldots,N$), each having in-plane susceptibility κ_i and z-coordinate d_i. Suppose this heterostructure is immersed in an isotropic medium of dielectric constant ϵ. In practice the dielectric constant is taken to be the average of the dielectric constants of the media above and below the heterobilayer.

Suppose that a test charge density

$$\rho^j_{\mathrm{tot}}(\mathbf{r},z) = \rho^j(\mathbf{r})\delta(z - d_j), \tag{A1}$$

is present in layer j. The resulting electric displacement field is

$$\mathbf{D} = -\frac{\epsilon}{4\pi}\nabla\phi(\mathbf{r},z) - \sum_i \kappa_i[\nabla_\parallel\phi(\mathbf{r},d_i)]\delta(z-d_i), \quad \text{(A2)}$$

where $\nabla_\parallel$ is the 2D gradient operator (excluding the z-component). Gauss's law yields

$$\rho^j(\mathbf{r},z)\delta(z-d_j) = -\frac{\epsilon}{4\pi}\nabla^2\phi(\mathbf{r},z) - \sum_i \kappa_i[\nabla_\parallel^2\phi(\mathbf{r},d_i)]\delta(z-d_i). \quad \text{(A3)}$$

Taking the Fourier transform gives

$$\rho^j(\mathbf{q})e^{-ikd_j} = \frac{\epsilon}{4\pi}(q^2+k^2)\phi(\mathbf{q},k) + q^2\sum_i \kappa_i\phi(\mathbf{q},d_i)e^{-ikd_i}, \quad \text{(A4)}$$

which, after Fourier inversion in the k variable only, gives

$$\rho^j(\mathbf{q})e^{-q|z-d_j|} = \frac{\epsilon}{2\pi}q\phi(\mathbf{q},z) + q^2\sum_i \kappa_i\phi(\mathbf{q},d_i)e^{-q|z-d_i|}. \quad \text{(A5)}$$

Evaluating Eq. (A5) at each layer ($z=d_l$, $l=\{1,2,\ldots,N\}$), we find

$$\rho^j(\mathbf{q})e^{-q|d_l-d_j|} = q[\epsilon/(2\pi)-\kappa_l q]\phi(\mathbf{q},d_l) + q^2\sum_{i\neq l}\kappa_i\phi(\mathbf{q},d_i)e^{-q|d_l-d_i|}, \quad \text{(A6)}$$

which is a matrix equation

$$\rho_l^j(\mathbf{q}) = \sum_i M_{li}(\mathbf{q})\phi_i(\mathbf{q}), \quad \text{(A7)}$$

where

$$\rho_l^j(\mathbf{q}) = \rho^j(\mathbf{q})e^{-q|d_l-d_j|},$$
$$\phi_i(\mathbf{q}) = \phi(\mathbf{q},d_i), \quad \text{(A8)}$$
$$M_{li} = \begin{cases} q[\epsilon/(2\pi)+\kappa_l q] & \text{if } i=l \\ q^2\kappa_i e^{-q|d_l-d_i|} & \text{otherwise} \end{cases}.$$

The solution to Eq. (A7) is a set of $\phi_i(\mathbf{q}) \equiv \rho^j(\mathbf{q}) \times v_{ji}(\mathbf{q})$, with $v_{ji}(\mathbf{q})$ being the Fourier components of the interaction potential between layer j and layer i. If $j=i$, then this is the intralayer interaction in layer j. This procedure should, in general, be repeated for $j=1,2,\ldots,N$; however, if there is sufficient symmetry (e.g., a mirror symmetry about a plane through the center of the heterostructure) then only a subset of j values will require explicit solution of Eq. (A7).

The same analysis can be shown to apply in the case that the surrounding dielectric medium is anisotropic, having dielectric tensor

$$\tilde{\epsilon} = \begin{pmatrix} \epsilon_\parallel & 0 & 0 \\ 0 & \epsilon_\parallel & 0 \\ 0 & 0 & \epsilon_\perp \end{pmatrix}, \quad \text{(A9)}$$

provided the substitutions

$$d_i \to D_i = \sqrt{\epsilon_\parallel/\epsilon_\perp}\,d_i, \quad \text{(A10)}$$
$$\epsilon \to \bar{\epsilon} = \sqrt{\epsilon_\parallel\epsilon_\perp}, \quad \text{(A11)}$$

are also made.

2. Numerical evaluation of the bilayer Keldysh interaction

In the bilayer case ($N=2$), it is straightforward to solve Eq. (A7) to obtain the intralayer ($\mathcal{V}$ and $\mathcal{V}'$) and interlayer ($\mathcal{W}$) potentials of Eqs. (1a)–(1c). Continuum QMC calculations require the potential energy to be evaluated in real space. We therefore require the inverse Fourier transforms of Eqs. (1a)–(1c), which reduce to Hankel transforms due to the circular symmetry of the interaction potentials.

At long range (small q), the intralayer interaction $\mathcal{V}(\mathbf{q}) = 2\pi/\{\epsilon q[1+(r_*+r_*')q]\} + O(q)$ reduces to the monolayer Keldysh form [19], with an effective screening length $r_*^{\text{eff}} = r_* + r_*'$. The inverse Fourier transform can be performed analytically in this limit, giving

$$\mathcal{V}(r) \approx \frac{\pi}{2\epsilon(r_*+r_*')}[H_0(r/(r_*+r_*')) - Y_0(r/(r_*+r_*'))] + O(r^{-3}), \quad \text{(A12)}$$

where H_0 and Y_0 are a Struve function and a Bessel function of the second kind, respectively. Equation (A12) is a good approximation at long range.

At short range (large q), the intralayer interaction of Eq. (1a) again reduces to the monolayer Keldysh form, but this time with $r_*^{\text{eff}} = r_*$, i.e., the second layer becomes irrelevant. On the other hand, at very long range, the monolayer Keldysh interaction is also valid, since $\mathcal{V}(\mathbf{q}) = 2\pi/(\epsilon q) + O(1)$ at small q so that the interaction is of Coulomb form. Thus the monolayer Keldysh interaction

$$\mathcal{V}(r) \approx \frac{\pi}{2\epsilon r_*^{\text{eff}}}[H_0(r/r_*^{\text{eff}}) - Y_0(r/r_*^{\text{eff}})] + O(r^{-2}) \quad \text{(A13)}$$

is a reasonable approximation to the intralayer interaction at *both* short and very long range.

To evaluate the "full" intralayer interaction numerically, we used the quadrature method of Ogata [45] to perform the Hankel transform of $\mathcal{V}(\mathbf{q}) - 2\pi/\{\epsilon q[1+r_* q]\}$, then added the result to the monolayer Keldysh interaction of Eq. (A13). Partitioning the interaction into a long-range part and a numerically evaluated short-range part ensures that the quadrature is relatively straightforward, and that we can introduce a cutoff at large r, beyond which the numerical corrective term is negligible.

At small q, the interlayer interaction of Eq. (1c) reduces to the displaced Coulomb form $\mathcal{W}(q) = 2\pi e^{-(r_*+r_*'+d)q}/(\epsilon q) + O(q)$; hence the long-range interlayer potential in real space is given by

$$\mathcal{W}(r) \approx \frac{1}{4\pi\sqrt{r^2+(r_*+r_*'+d)^2}} + O(r^{-3}). \quad \text{(A14)}$$

At short range in real space the interlayer interaction should be nondivergent. Equation (A14) satisfies this qualitative requirement. To evaluate the "full" interlayer interaction numerically, we performed the numerical Hankel transform of $\mathcal{W}(\mathbf{q}) - 2\pi e^{-(r_*+r_*'+d)q}/(\epsilon q)$, then added the result to Eq. (A14).

There is an alternative long-range approximation to the interlayer potential, which is more like the intralayer potential. Noting that $\mathcal{W}(\mathbf{q}) = 2\pi/\{\epsilon q[1+(r_*+r_*'+d)q]\} + O(q)$, the long-range interlayer potential reduces to a Keldysh

potential with $r_*^{\rm eff} = r_* + r_*' + d$, giving

$$\mathcal{W}(r) \approx \frac{\pi}{2\epsilon(r_* + r_*' + d)} \times \left[H_0\left(\frac{r}{r_* + r_*' + d}\right) - Y_0\left(\frac{r}{r_* + r_*' + d}\right)\right] + O(r^{-3}). \quad \text{(A15)}$$

This introduces unphysical singular behavior into the interlayer interaction at short range.

APPENDIX B: QMC CALCULATIONS

1. Technical details

We performed VMC and DMC calculations [16,17] for complexes of distinguishable charge carriers and fixed ions interacting via the "full" bilayer potential [Eqs. (1a)–(1c)] and the approximate small-q Keldysh form of the potential [Eqs. (A12) and (A15)], as described in Appendix A 2. We used trial wave functions of Jastrow form, where the Jastrow exponents contained smoothly truncated polynomial particle-particle terms, ion-particle terms, ion-particle-particle, and particle-particle-particle terms [46,47]. Additional terms satisfying the analogs of the Kato cusp conditions [6,20,48] were applied to the trial wave function between pairs of particles wherever there was a logarithmic divergence in the interaction between them, including the unphysical divergences in the approximate Keldysh interaction. Free parameters were optimized using VMC with variance [49,50] and energy minimization [51] as implemented in the CASINO code [52].

In our DMC calculations, we used two DMC time steps in the ratio 1:4 and the corresponding target populations in the ratio 4:1, allowing a simultaneous extrapolation to zero time step and infinite population. Since the charge carriers are distinguishable, there is no fixed-node error and hence DMC provides exact ground-state solutions to the effective-mass model of interacting charge carriers with the chosen model interaction.

2. Energies of complexes in the hBN/$MoSe_2$/WSe_2/hBN heterostructure

Table IV shows the total energies of charge-carrier complexes in the hBN/$MoSe_2$/WSe_2/hBN heterostructure. For completeness we include results in which the electrons are found in either layer; however, the results of immediate relevance to this paper are those for which the electrons are all found in the $MoSe_2$ layer. DMC results for two-particle complexes agree with calculations performed using Mathematica's finite-element method [53] (see Appendix E). Using total energies, one can assess the most energetically favorable dissociations (see Table V) and therefore calculate the binding energies of the various complexes.

It is clear from Table V that the approximate Keldysh interaction performs well at calculating binding energies provided the dissociation does not involve significant changes to short-range pair distributions. As an extreme case, the binding energy of an exciton, which is simply equal to its total energy and hence does not benefit from any cancellation of errors, is overestimated by 23% when the approximate Keldysh interaction is used. We are not aware of any published experimental results on donor-bound interlayer complexes in heterobilayers, but we discuss the validity of our results for intralayer complexes in Appendix B 4.

TABLE V. Dissociations of complexes and the associated binding energies in hBN/$MoSe_2$/WSe_2/hBN. The naming convention for the carrier complexes is explained in the caption of Table IV.

Dissociation process		Binding energy (meV) Appr. Kel.	Bilayer pot.
$X^-_{vc'c'}$	$\to X_{vc'} + e_{c'}$	4.2380(4)	4.09(3)
$X^+_{vvc'}$	$\to X_{vc'} + h_v$		3.89(2)
$X_{vc'}X_{vc'}$	$\to X_{vc'} + X_{vc'}$		unbound
$X_{vc'}X^-_{vc'c'}$	$\to X_{vc'} + X^-_{vc'c'}$		unbound
$D^-_{c'c'}$	$\to D^0_{c'} + e_{c'}$	13.6948(3)	20.57(1)
$D^0_{c'}h_v$	$\to D^0_{c'} + h_v$	0.2340(8)	unbound
$D^0_{c'}X_{vc'}$	$\to X_{vc'} + D^0_{c'}$	11.52(2)	22.516(4)
$D^0_{c'}X^+_{vvc'}$	$\to D^0_{c'} + X^+_{vvc'}$		23.74(2)
$D^-_{c'c'}X_{vc'}$	$\to X_{vc'} + D^-_{c'c'}$	11.93(1)	9.43(4)
$D^0_{c'}X_{vc'}X_{vc'}$	$\to D^0_{c'}X_{vc'} + X_{vc'}$		unbound
$D^-_{c'c'}X_{vc'}X_{vc'}$	$\to D^-_{c'c'}X_{vc'} + X_{vc'}$		3.3(2)
A^+_{vv}	$\to A^0_v + h_v$		18.32(1)
$A^0_v e_{c'}$	$\to A^0_v + e_{c'}$		unbound
$A^0_v X_{vc'}$	$\to A^0_v + X_{vc'}$		19.938(4)
$A^0_v X^-_{vc'c'}$	$\to A^0_v + X^-_{vc'c'}$		21.46(3)
$X^-_{vcc'}$	$\to X_{vc} + e_{c'}$	6.0000(5)	unbound
X^-_{vcc}	$\to X_v + e_c$	9.1170(5)	11.83(1)
$D^0_{c'}X_{vc}$	$\to X_{vc} + D^0_{c'}$	1.926(5)	unbound
$D^-_{c'c'}X_{vc}$	$\to X_{vc} + D^-_{c'c'}$	10.26(1)	unbound
$D^-_{cc'}$	$\to D^0_{c'} + e_c$	2.6020(5)	unbound
$D^0_{c'}X^-_{vcc}$	$\to D^0_{c'} + X^-_{vcc}$	8.03(1)	unbound
D^-_{cc}	$\to D^0_c + e_c$	4.4297(9)	unbound
D^+X_{vc}	$\to D^+ + X_{vc}$	19.156(2)	1.286(8)

3. Sensitivity to model parameters

We have performed test calculations to determine the sensitivity of the DMC-evaluated $D^0_{c'}X_{vc'}$ binding energy to the model parameters $m_{c'}$, m_v, r_*, r_*', and d in the hBN-encapsulated heterobilayer. Note that r_* and r_*' are here the screening-length parameters in vacuum, so that the screening lengths in a dielectric environment are r_*/ϵ and r_*'/ϵ. We find that, upon variation of each of the parameters in turn by $\pm 10\%$ from the values listed in Table I, the $D^0_{c'}X_{vc'}$ binding energy never varies by more than 8% (1.8 meV), as shown in Table VI. The derivatives of the binding energy with respect to the parameters were evaluated numerically by the central difference approximation. Nondimensionalizing lengths by the exciton Bohr radius and energies by the exciton Rydberg [23], it is easy to show that the derivative of a binding energy $\mathcal{E}^{\rm b}$ with respect to the dielectric constant is

$$\frac{\partial \mathcal{E}^{\rm b}}{\partial \epsilon} = -\frac{1}{\epsilon}\left(2r_*\frac{\partial \mathcal{E}^{\rm b}}{\partial r_*} + 2r_*'\frac{\partial \mathcal{E}^{\rm b}}{\partial r_*'} + d\frac{\partial \mathcal{E}^{\rm b}}{\partial d} + 2\mathcal{E}^{\rm b}\right), \quad \text{(B1)}$$

allowing us to evaluate the sensitivity of the binding energy with respect to the dielectric constant. We find that the binding energies are most sensitive to the screening parameter r_*, followed by the dielectric constant ϵ, followed by the electron and hole masses $m_{c'}$ and m_v, and that the sensitivity to the layer

TABLE VI. Derivatives of DMC binding energies $\mathcal{E}^{\mathrm{b}}_{\mathrm{D}^0_{c'}X_{vc'}}$ of the interlayer donor-bound trion under variations δP of different model parameters P. With the exception of the dielectric constant ϵ, the parameters are varied by $\pm 10\%$ about the values listed in Table I and the central difference approximation is used to estimate the derivative with respect to the parameter value. The binding energy when all the parameters take the values listed in Table I is $\mathcal{E}^{\mathrm{b}}_{\mathrm{D}^0_{c'}X_{vc'}} = 22.516(4)$ meV. Note that r_* and r'_* are here the screening lengths for a monolayer in vacuum. The derivative of the binding energy with respect to the dielectric constant ϵ was evaluated by the chain rule, as described in the text.

P	δP	$\mathcal{E}^{\mathrm{b}}_{\mathrm{D}^0_{c'}X_{vc'}}$ (meV)	$\partial\mathcal{E}^{\mathrm{b}}_{\mathrm{D}^0_{c'}X_{vc'}}/\partial P$
$m_{c'}$	$+10\%$	23.27(1)	20.7 meV/m_0
	-10%	21.70(1)	
m_v	$+10\%$	22.71(1)	6.20 meV/m_0
	-10%	22.29(1)	
r_*	$+10\%$	20.96(1)	-0.421 meV/Å
	-10%	24.31(1)	
r'_*	$+10\%$	22.46(1)	-0.00691 meV/Å
	-10%	22.52(1)	
d	$+10\%$	22.93(1)	0.705 meV/Å
	-10%	22.02(1)	
ϵ	$+10\%$	∼20.97	-3.87 meV
	-10%	∼24.06	

separation d is relatively weak. The sensitivity to the screening parameter r'_* is very weak in the present case, because only one hole resides in the WSe_2 layer.

We have also performed DMC calculations with $\epsilon = 4.5$ (instead of $\epsilon = 4$), finding that the $X_{vc'}$, $X^-_{vc'c'}$, $\mathrm{D}^0_{c'}$, and $\mathrm{D}^0_{c'}X_{vc'}$ binding energies are 76, 3.8, 207, and 20.7 meV, respectively. This directly confirms that the sensitivity to the precise value of the dielectric constant of the environment is relatively weak. The value of $\partial\mathcal{E}^{\mathrm{b}}_{\mathrm{D}^0_{c'}X_{vc'}}/\partial\epsilon$ found by the forward difference approximation is -3.63 meV, which is in reasonable agreement with the value obtained using the chain rule, reported in Table VI.

4. Comparison of intralayer binding energies with experimental results

For TMD monolayers, experimental agreement with QMC calculations of the binding energies of charge-carrier complexes employing the Keldysh interaction has previously been addressed in Refs. [6,23]. Trion binding energies are found to be in excellent agreement with experimental results.

Relatively few experimental studies of charge-carrier complexes in heterobilayers have been performed to date. Ceballos *et al.* studied a $SiO_2/MoSe_2/MoS_2$/vacuum sample [54], performing PL measurements on monolayer $MoSe_2$, monolayer MoS_2, and heterobilayer $MoSe_2/MoS_2$ regions of their sample. Gong *et al.* studied a $SiO_2/MoS_2/WS_2$/vacuum sample [55], again performing PL measurements on each of the three distinct surface regions. Both experiments, although studying different TMD bilayers prepared by different means, observed only small shifts in the dominant intralayer exciton lines on moving from monolayer regions to bilayer regions. Our heterobilayer results of Table V, in conjunction with monolayer binding-energy fitting formulas presented in Ref. [23] provide further support for this claim. The intralayer exciton energy reported in Table IV for an exciton X_{vc} in the WSe_2 layer of a hBN/$MoSe_2$/WSe_2/hBN heterostructure is -140.4 meV, whereas the exciton total energy in monolayer WSe_2 encapsulated in hBN is -159.7 meV, according to the monolayer fitting formula. The intralayer negative trion X^-_{vcc} binding energy reported in Table V is 11.8 meV, whereas the fitted negative-trion binding energy in monolayer WSe_2 encapsulated in hBN is 13.6 meV. Thus the intralayer exciton energy differs by about 19 meV from the monolayer exciton energy, while the intralayer trion binding energy differs by about 2 meV from the monolayer result.

In summary, intralayer binding energies in a heterobilayer are very similar to monolayer binding energies, and hence the validity of our model may be judged by examining previously reported results for TMD monolayers [6,23].

5. Calculation of the overlap integrals

a. VMC evaluation of the normalization integral of a many-body wave function

Consider a complex of N quantum particles with unnormalized wave function $\Phi(\mathbf{R})$, where $\mathbf{R} = (\mathbf{r}_1, \ldots, \mathbf{r}_N)$ is the $2N$-dimensional vector of all particle coordinates. Let $\Psi(\mathbf{R})$ be a normalized, bound-state sampling wave function, which ideally has a large overlap with Φ and the same asymptotic behavior. Then

$$\int |\Phi(\mathbf{R})|^2\, d^{2N}\mathbf{R} = \int |\Psi(\mathbf{R})|^2 \left|\frac{\Phi(\mathbf{R})}{\Psi(\mathbf{R})}\right|^2 d^{2N}\mathbf{R} = \left\langle \left|\frac{\Phi(\mathbf{R})}{\Psi(\mathbf{R})}\right|^2 \right\rangle_{|\Psi|^2}. \tag{B2}$$

Hence we can evaluate the normalization of Φ by VMC sampling of $|\Psi(\mathbf{R})|^2$. We used the simple Jastrow form

$$\Psi(\mathbf{R}) = \prod_{i=1}^{N} \left(\sqrt{\frac{2}{\pi}} c e^{-c r_i}\right) \tag{B3}$$

for the sampling wave function, where the exponent c is a positive, adjustable parameter that was chosen to maximize the efficiency of the calculation.

b. Evaluation of overlap integrals

Numerical estimates of the various overlap integrals in the expressions for the radiative recombination rates of donor-bound trions in a hBN/$MoSe_2$/WSe_2/hBN system are reported in Table VII. The ground state $\chi_{1s}(\mathbf{r}_e)$ and the first excited state $\chi_{2s}(\mathbf{r}_e)$ of the neutral donor atom ($\mathrm{D}^0_{c'}$) were calculated using a finite-element method (see Appendix E). Using a VMC-optimized trial wave function $\Phi(\mathbf{r}_h, \mathbf{r}_{e_1}, \mathbf{r}_{e_2})$ for the ground state of the donor-bound negative trion ($\mathrm{D}^0_{c'}X_{vc'}$), we employed a grid-based method to evaluate those overlap integrals in Table VII that can be reduced to one-dimensional radial integrals. The remaining integrals were evaluated by a VMC method, as described below.

Let Ψ be a sampling wave function, as defined in Appendix B 5 a. The overlap of the trion wave function with the donor-atom wave function when an electron and a hole are

TABLE VII. Overlap integrals required for calculations of radiative recombination rates. Calculations are performed for a hBN/$MoSe_2$/WSe_2/hBN system. $\Phi(\mathbf{r}_h,\mathbf{r}_{e1},\mathbf{r}_{e2})$ is the ground-state wave function of the donor-bound negative trion, with both donor and electrons in the $MoSe_2$ layer and the hole in the WSe_2 layer ($D^0_{c'}X_{vc'}$). $\chi_{1s}(\mathbf{r}_e)$ and $\chi_{2s}(\mathbf{r}_e)$ are the ground-state and first-excited-state (rotationally invariant) wave functions of the neutral donor atom in the $MoSe_2$ layer ($D^0_{c'}$).

Overlap	Approx. Keldysh	Bilayer pot.
$\frac{\lvert\Phi(\mathbf{0},\mathbf{0},\mathbf{0})\rvert^2}{\int\lvert\Phi\rvert^2\,d^6\mathbf{R}}$	1.29×10^{-9} Å^{-6}	2.75×10^{-9} Å^{-6}
$\frac{\lvert\int\Phi(\mathbf{r},\mathbf{r},\mathbf{0})\,d^2\mathbf{r}\rvert^2}{\int\lvert\Phi\rvert^2\,d^6\mathbf{R}}$	8.09×10^{-3} Å^{-2}	6.08×10^{-3} Å^{-2}
$\frac{\int\lvert\Phi(\mathbf{r},\mathbf{r},0)\rvert^2\,d^2\mathbf{r}}{\int\lvert\Phi\rvert^2\,d^6\mathbf{R}}$	1.28×10^{-6} Å^{-4}	1.38×10^{-6} Å^{-4}
$\frac{\int\lvert\Phi(\mathbf{r},\mathbf{r},\mathbf{r})\rvert^2\,d^2\mathbf{r}}{\int\lvert\Phi\rvert^2\,d^6\mathbf{R}}$	3.22×10^{-7} Å^{-4}	2.37×10^{-7} Å^{-4}
$\frac{\lvert\int\chi_{1s}(\mathbf{r})\Phi(\mathbf{0},\mathbf{0},\mathbf{r})\,d^2\mathbf{r}\rvert^2}{\int\lvert\Phi\rvert^2\,d^6\mathbf{R}\times\int\lvert\chi_{1s}\rvert^2\,d^2\mathbf{r}}$	6.94×10^{-7} Å^{-4}	1.21×10^{-6} Å^{-4}
$\frac{\lvert\iint\chi_{1s}(\mathbf{r}')\Phi(\mathbf{r},\mathbf{r},\mathbf{r}')\,d^2\mathbf{r}\,d^2\mathbf{r}'\rvert^2}{\int\lvert\Phi\rvert^2\,d^6\mathbf{R}\times\int\lvert\chi_{1s}\rvert^2\,d^2\mathbf{r}}$	3.54	1.47
$\frac{\int\lvert\int\chi_{1s}(\mathbf{r}')\Phi(\mathbf{r},\mathbf{r},\mathbf{r}')\,d^2\mathbf{r}'\rvert^2d^2\mathbf{r}}{\int\lvert\Phi\rvert^2\,d^6\mathbf{R}\times\int\lvert\chi_{1s}\rvert^2\,d^2\mathbf{r}}$	5.90×10^{-4} Å^{-2}	3.85×10^{-4} Å^{-2}
$\frac{\lvert\int\chi_{2s}(\mathbf{r})\Phi(\mathbf{0},\mathbf{0},\mathbf{r})\,d^2\mathbf{r}\rvert^2}{\int\lvert\Phi\rvert^2\,d^6\mathbf{R}\times\int\lvert\chi_{2s}\rvert^2\,d^2\mathbf{r}}$	2.01×10^{-8} Å^{-4}	1.13×10^{-7} Å^{-4}
$\frac{\lvert\iint\chi_{2s}(\mathbf{r}')\Phi(\mathbf{r},\mathbf{r},\mathbf{r}')\,d^2\mathbf{r}\,d^2\mathbf{r}'\rvert^2}{\int\lvert\Phi\rvert^2\,d^6\mathbf{R}\times\int\lvert\chi_{2s}\rvert^2\,d^2\mathbf{r}}$	0.0379	0.0254
$\frac{\int\lvert\int\chi_{2s}(\mathbf{r}')\Phi(\mathbf{r},\mathbf{r},\mathbf{r}')\,d^2\mathbf{r}'\rvert^2d^2\mathbf{r}}{\int\lvert\Phi\rvert^2\,d^6\mathbf{R}\times\int\lvert\chi_{2s}\rvert^2\,d^2\mathbf{r}}$	1.04×10^{-5} Å^{-2}	1.89×10^{-5} Å^{-2}

pinned vertically above one another is

$$\begin{aligned}&\iint\chi^*(\mathbf{r}_1)\Phi(\mathbf{r}_2,\mathbf{r}_2,\mathbf{r}_1)\,d^2\mathbf{r}_1\,d^2\mathbf{r}_2\\&=\int|\Psi(\mathbf{R})|^2\frac{\chi^*(\mathbf{r}_2)\Phi(\mathbf{r}_1,\mathbf{r}_2,\mathbf{r}_1)}{|\Psi(\mathbf{R})|^2}\,d^4\mathbf{R}\\&=\left\langle\frac{\chi^*(\mathbf{r}_2)\Phi(\mathbf{r}_1,\mathbf{r}_2,\mathbf{r}_1)}{|\Psi(\mathbf{R})|^2}\right\rangle_{|\Psi|^2}.\end{aligned}\tag{B4}$$

The last expression can readily be evaluated by VMC sampling of $|\Psi|^2$, using accurate numerical representations of the donor-atom wave function $\chi(\mathbf{r}_e)$ obtained in the finite-element calculations. The overlap integrals are precise to at least three significant figures; however, there is an unknown error arising from the fact that the trial wave function $\Phi(\mathbf{r}_h,\mathbf{r}_{e_1},\mathbf{r}_{e_2})$ only approximates the exact ground state.

APPENDIX C: RADIATIVE RECOMBINATION ASSISTED BY SHORT-RANGE COULOMB INTERACTIONS

Consider the wave function $\chi(\mathbf{r})$ for $D^0_{c'}$ complexes in the long-range (Keldysh) approximation described in Sec. IV. The complex state can be written in the form of Eq. (12), with the substitution $\tilde{\chi}_{\mathbf{k}}\longrightarrow\tilde{\chi}^0_{\mathbf{k}}$, and short-range electrostatic interactions and interlayer tunneling can be treated as perturbations to this initial state. Setting $\tau'=\tau$ and $\sigma'=\sigma$ in Eq. (12), radiative decay is determined by the matrix element $\langle\tau,\mathbf{q}|\hat{H}_r|D^0;\mathbf{k}_h\rangle^{(2)}$, where $|\tau,\mathbf{q}\rangle=a^\dagger_\tau(\mathbf{q})|\Omega\rangle$ is the final state in which a photon of momentum $\mathbf{q}$ and the appropriate polarization τ has been emitted after recombination of the bound electron with the delocalized hole. The notation $|A\rangle^{(2)}$ indicates that the state includes corrections up to second order in perturbation theory, in this case from the interlayer tunneling ($\hat{H}_t$) and short-range interaction ($\hat{U}^{>}_{\text{intra}}$) terms.

The diagrams of Fig. 3 correspond to those corrections to the wave function that are relevant for radiative recombination in the large-twist-angle regime, where $\mathcal{E}^b_{D^0}\ll\frac{\hbar^2\Delta K^2}{2m_\alpha}$. Following the order of the diagrams in the figure, and assuming that $k_h,q\ll\Delta K$, the optical matrix element for $D^0_{c'}h_v$ recombination is given in terms of the real-space impurity wave function by

$$\begin{aligned}\langle\tau,\mathbf{q}|\hat{H}_r|D^0;\mathbf{k}_h\rangle^{(2)}=&\sum_{n=0}^{2}\frac{6\pi e^3e^{-i\mathbf{G}_n\cdot\mathbf{r}_0}\chi(0)}{\epsilon\,r'_*S\left(C_3^n\Delta\mathbf{K}\right)^2}\sqrt{\frac{4\pi\hbar c}{L\sqrt{q_\perp^2+q_\parallel^2}}}\\&\times\left[-\frac{\gamma t_{cc}/\hbar c}{\left(\mathcal{E}^b_{D^0}+\Delta_c\right)\left(\mathcal{E}^b_{D^0}+\frac{\hbar^2(C_3^n\Delta\mathbf{K})^2}{2m_{c'}}\right)}+\frac{\gamma' t_{vv}/\hbar c}{\left(\mathcal{E}^b_{D^0}+\Delta_v+\frac{\hbar^2(C_3^n\Delta\mathbf{K})^2}{2m_{c'}}+\frac{\hbar^2(C_3^n\Delta\mathbf{K})^2}{2m_{v'}}\right)\left(\mathcal{E}^b_{D^0}+\frac{\hbar^2(C_3^n\Delta\mathbf{K})^2}{2m_{c'}}\right)}\right.\\&\left.-\frac{\gamma' t_{vv}/\hbar c}{\Delta_v\left(\Delta_v+\frac{\hbar^2(C_3^n\Delta\mathbf{K})^2}{2m_{v'}}\right)}+\frac{\gamma' t_{vv}/\hbar c}{\left(\mathcal{E}^b_{D^0}+\Delta_v+\frac{\hbar^2(C_3^n\Delta\mathbf{K})^2}{2m_{c'}}+\frac{\hbar^2(C_3^n\Delta\mathbf{K})^2}{2m_{v'}}\right)\left(\Delta_v+\frac{\hbar^2(C_3^n\Delta\mathbf{K})^2}{2m_{v'}}\right)}\right],\end{aligned}\tag{C1}$$

where the Bragg vectors $\mathbf{G}_n$ and valley mismatch momenta $C_3^n\Delta\mathbf{K}=\Delta\mathbf{K}+(\mathbf{G}'_n-\mathbf{G}_n)$ are shown in Fig. 10. The matrix element in Eq. (C1) can be written in terms of the stacking-dependent function $F(\mathbf{r}_0)=1+e^{-i\mathbf{G}_1\cdot\mathbf{r}_0}+e^{-i\mathbf{G}_2\cdot\mathbf{r}_0}$ (see Fig. 10). We additionally assume that the CB and VB spacings remain a large scale in the problem, such that $\frac{\hbar^2\Delta K^2}{2m_\alpha}\ll\Delta_c,\Delta_v$. In this approximation, the third and fourth terms in Eq. (C1) cancel out, corresponding to the diagrams in Figs. 3(c) and 3(d). Substituting the resulting expression into Eq. (11) gives Eq. (18), where the probability that the hole state is occupied is introduced through the hole density $N(\mathbf{k}_h)$. This analysis can be carried out for $D^0_{c'}X_{vc'}$ complexes, yielding Eqs. (19) and (20).

The large momentum components introduced by the short-range interaction terms are irrelevant in the small-twist-angle regime, which is dominated by the small momentum sector of the wave function. In this case, the optical matrix element is obtained from the perturbed state $|D^0;\mathbf{k}_h\rangle^{(1)}$, including

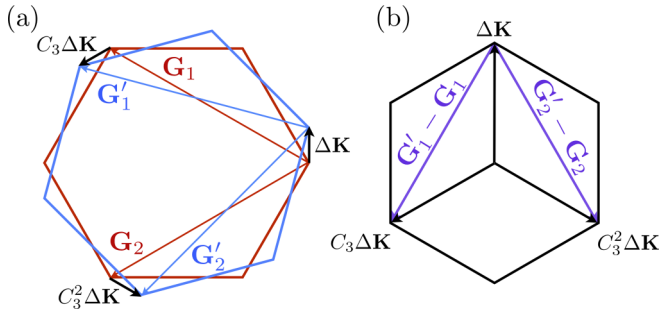

FIG. 10. (a) Reciprocal lattice vectors $\mathbf{G}_n$ and $\mathbf{G}_n'$ of the two layers, and valley mismatch vectors $C_3^n\Delta\mathbf{K}$ ($n = 0, 1, 2$), with the convention $\mathbf{G}_0 = \mathbf{G}_0' = 0$. (b) The vectors $C_3^n\Delta\mathbf{K}$ are connected by $\mathbf{G}_n' - \mathbf{G}_n$.

first-order tunneling corrections [Eq. (10)]. The optical matrix element is

$$\langle\tau,\mathbf{q}|\hat{H}_r|\mathrm{D}^0;\mathbf{k}_h\rangle = \sum_{n=0}^{2}\int d^2r\,\frac{e^{i(C_3^n\Delta\mathbf{K}+\mathbf{k}_h+\mathbf{q})\cdot\mathbf{r}}}{\sqrt{S}}\chi(\mathbf{r}) \times\sqrt{\frac{4\pi\,\hbar c e^2}{SLq}}\left[\frac{t_{vv}\gamma'}{\hbar c\,\Delta_v} - \frac{t_{cc}\gamma}{\hbar c\left(\Delta_c + \mathcal{E}_{\mathrm{D}^0}^{\mathrm{b}}\right)}\right]e^{-i\mathbf{G}_n\cdot\mathbf{r}_0}. \quad \text{(C2)}$$

Substituting into Eq. (11) leads to Eq. (13), and similar procedures are used to obtain Eq. (15) for $\mathrm{D}^0_{c'}X_{vc'}$ complexes.

Notice that the second radiative channel for $\mathrm{D}^0_{c'}X_{vc'}$ discussed in the main text does not apply to this regime. The small-twist-angle analogue to the recoil process due to electron-electron interactions involves a small momentum transfer, and is thus already contained in the unperturbed state $|\mathrm{D}^0\mathrm{X}\rangle$.

APPENDIX D: PHONON EFFECTS ON RADIATIVE RECOMBINATION

The discussion of Appendix C can easily be adapted to e-ph interactions, $\hat{H}_{\text{e-ph}}$ [Eq. (21)]. In the following we adopt the assumptions introduced in Appendix C; namely, $\frac{\hbar^2\Delta K^2}{2m_\alpha}$, $\mathcal{E}_{\mathrm{D}^0}^{\mathrm{b}} \ll \Delta_c, \Delta_v$. In addition, we use $\hbar\omega_{\Lambda,\nu}(\xi) \ll \Delta_c, \Delta_v$, which is always valid in our cases of interest.

In the large-twist-angle regime, consider the process whereby the electron in a $\mathrm{D}^0_{c'}$ bridges the valley mismatch by emitting a phonon in mode ν and momentum $\boldsymbol{\xi}$, with $\boldsymbol{\xi} \sim \Delta\mathbf{K}$, in either the electron ($\Lambda = \mathrm{e}$) or hole ($\Lambda = \mathrm{h}$) layer. The electron recombines with a delocalized hole of momentum $\mathbf{k}_h$, emitting a photon of momentum $\mathbf{q}$ and polarization μ, leading to the final state

$$|\tau,\mathbf{q};\nu,\boldsymbol{\xi}\rangle_\Lambda = a_\tau^\dagger(\mathbf{q})b_{\Lambda,\nu,-\boldsymbol{\xi}}^\dagger|\Omega\rangle. \quad \text{(D1)}$$

Considering the phonon energies presented in Table V, in this regime we have $\frac{\hbar^2\Delta K^2}{2m_\alpha} \gg \hbar\omega_{\Lambda,\nu}$, and the radiative matrix elements with phonon emission can be approximated by

$${}_{\mathrm{h}}\langle\tau,\mathbf{q};\nu,\boldsymbol{\xi}|\hat{H}_r|\mathrm{D}^0;\mathbf{k}_h\rangle \approx \frac{\tilde{\chi}\left(\mathbf{k}_h+\boldsymbol{\xi}-C_3^n\Delta\mathbf{K}\right)}{S}g_{v,\nu}(\Delta K)\sqrt{\frac{4\pi\hbar c}{SLq}}\frac{\gamma' t_{vv}}{\hbar c\,\Delta_v}\left[\frac{2m_v}{\hbar^2\Delta K^2} - \frac{2m_{c'}}{\hbar^2\Delta K^2}\right]e^{-i\mathbf{G}_n\cdot\mathbf{r}_0}, \quad \text{(D2a)}$$

$${}_{\mathrm{e}}\langle\tau,\mathbf{q};\nu,\boldsymbol{\xi}|\hat{H}_r|\mathrm{D}^0;\mathbf{k}_h\rangle \approx \frac{\tilde{\chi}\left(\mathbf{k}_h+\boldsymbol{\xi}-C_3^n\Delta\mathbf{K}\right)}{S}g_{c',\nu}(\Delta K)\sqrt{\frac{4\pi\hbar c}{SLq}}\frac{\gamma t_{cc}}{\hbar c\,\Delta_c}\left[\frac{6m_{c'}}{\hbar^2\Delta K^2} - \frac{6m_v}{\hbar^2\Delta K^2}\right]e^{-i\mathbf{G}_n\cdot\mathbf{r}_0}. \quad \text{(D2b)}$$

For large twist angle, finite values of the wave function are obtained only if $\boldsymbol{\xi} \approx C_3^n\Delta\mathbf{K}$, resulting in three final phonon states distinguishable by the direction of their momenta, and interference effects are lost. Furthermore, when substituting Eqs. (D2a) and (D2b) into the golden rule [Eq. (11)], the stacking-dependent phases also disappear. The result is Eq. (24a), and a similar procedure leads to Eq. (24b) for the phonon-assisted decay of $\mathrm{D}^0_{c'}X_{vc'}$ complexes.

The situation is more subtle in the small-twist-angle regime, where interference effects are restored in processes within the hole layer, and $\hbar\omega_{\Lambda,\nu} \lesssim \hbar^2\Delta K^2/(2m_\alpha)$, such that the phonon dispersion becomes important. The optical matrix elements are

$${}_{\mathrm{h}}\langle\tau,\mathbf{q};\boldsymbol{\xi},\nu|\hat{H}_r|\mathrm{D}^0;\mathbf{k}_h\rangle \approx \sum_{n=0}^{2}\frac{\tilde{\chi}\left(\mathbf{k}+\boldsymbol{\xi}-C_3^n\Delta\mathbf{K}\right)}{S}\sqrt{\frac{4\pi\hbar c}{SLq}}\left[\frac{\gamma' t_{vv}\,g_{v,\nu}(\boldsymbol{\xi})}{\hbar c\,\Delta_v\left(\frac{\hbar^2\xi^2}{2m_v}+\hbar\omega_\nu(\boldsymbol{\xi})\right)} - \frac{\gamma t_{cc}\,g_{v,\nu}(\boldsymbol{\xi})}{\hbar c\,\Delta_c\left(\frac{\hbar^2\xi^2}{2m_v}+\hbar\omega_\nu(\boldsymbol{\xi})+\mathcal{E}_{\mathrm{D}^0}^{\mathrm{b}}\right)}\right]e^{-i\mathbf{G}_n\cdot\mathbf{r}_0}, \quad \text{(D3)}$$

$${}_{\mathrm{e}}\langle\tau,\mathbf{q};\boldsymbol{\xi},\nu|\hat{H}_r|\mathrm{D}^0;\mathbf{k}_h\rangle = \sum_{n=0}^{2}\frac{\tilde{\chi}\left(\mathbf{k}+\boldsymbol{\xi}-C_3^n\Delta\mathbf{K}\right)}{S}\sqrt{\frac{4\pi\hbar c}{SLq}}\left[\frac{\gamma t_{cc}g_{v,c'}(\boldsymbol{\xi})}{\hbar c\,\Delta_c\left(\hbar\omega_\nu(\boldsymbol{\xi})+\mathcal{E}_{\mathrm{D}^0}^{\mathrm{b}}\right)} - \frac{\gamma' t_{vv}g_{v,c'}(\boldsymbol{\xi})}{\hbar c\,\Delta_v\left(\hbar\omega_\nu(\boldsymbol{\xi})+\mathcal{E}_{\mathrm{D}^0}^{\mathrm{b}}\right)}\right]e^{-i\mathbf{G}_n\cdot\mathbf{r}_0}. \quad \text{(D4)}$$

Following Ref. [31], we use $t_{cc} \ll t_{vv}$ to simplify these expressions. Using Fermi's golden rule and integrating over the photon momentum, we obtain the decay rates

$$\Gamma_{\mathrm{D}^0\mathrm{h}}^{<,\nu} \approx \sum_{\boldsymbol{\xi}}\left[\frac{|F(\mathbf{r}_0)|^2|g_{v,\nu}(0)|^2}{\left(\frac{\hbar^2\xi^2}{2m_v}+\hbar\omega_\nu\right)^2} + \frac{3|g_{c',\nu}(0)|^2}{\left(\hbar\omega_\nu+\mathcal{E}_{\mathrm{D}^0}^{\mathrm{b}}\right)^2}\right]\int d^2r\int d^2r'\,e^{i(\boldsymbol{\xi}-\Delta\mathbf{K})\cdot(\mathbf{r}'-\mathbf{r})}\chi(\mathbf{r})\chi^*(\mathbf{r}') \times\frac{e^2}{\hbar c}\frac{4\tilde{E}_g n_h}{\hbar\,S}\left[\frac{\gamma' t_{vv}}{\hbar c\,\Delta_v}\right]^2;\ \nu = \mathrm{LO},\mathrm{HP}, \quad \text{(D5a)}$$

$$\Gamma^{<,\mathrm{LA}}_{\mathrm{D^0h}} \approx \sum_{\boldsymbol{\xi}} \left[\frac{|F(\mathbf{r}_0)|^2 |g_{v,\mathrm{LA}}(\boldsymbol{\xi})|^2}{\left(\frac{\hbar^2\xi^2}{2m_v} + \hbar\, c_{\mathrm{LA}}\xi\right)^2} + \frac{3|g_{c',\mathrm{LA}}(\boldsymbol{\xi})|^2}{\mathcal{E}^{\mathrm{b}\,2}_{\mathrm{D^0}}} \right] \int d^2r \int d^2r'\, \mathrm{e}^{i\boldsymbol{\xi}\cdot(\mathbf{r}'-\mathbf{r})} \chi(\mathbf{r})\chi^*(\mathbf{r}') \times \frac{e^2}{\hbar c} \frac{4\tilde{E}_{\mathrm{g}} n_{\mathrm{h}}}{\hbar\, S} \left[\frac{\gamma' t_{vv}}{\hbar c\, \Delta_v}\right]^2, \tag{D5b}$$

for optical and acoustic phonon modes, respectively.

The divergence at $\xi = 0$ in Eq. (D5b) makes the first term dominant in the sum over $\boldsymbol{\xi}$, and we can neglect the second. The sum can be evaluated exactly in the continuous limit. Defining $\mathcal{F}(x) = -x[Y_1(x) + H_{-1}(x)]$, where $H_n(x)$ and $Y_n(x)$ are the nth Struve function and Bessel function of the second kind, respectively, we obtain

$$\Gamma^{<,\mathrm{LA}}_{\mathrm{D^0h}} \approx \frac{e^2}{\hbar c} \frac{\Xi_v^2\, \tilde{E}_{\mathrm{g}} m_v n_{\mathrm{h}}}{\hbar^3 \rho c_{\mathrm{LA}}^2} \left[\frac{\gamma' t_{vv}}{\hbar c\, \Delta_v}\right]^2 |F(\mathbf{r}_0)|^2 \int d^2r \int d^2r' \times \mathrm{e}^{i\boldsymbol{\xi}\cdot(\mathbf{r}'-\mathbf{r})} \chi(\mathbf{r})\chi^*(\mathbf{r}') \mathcal{F}\left(\frac{2m_v \hbar c_{\mathrm{LA}} |\mathbf{r}' - \mathbf{r}|}{\hbar^2}\right). \tag{D6}$$

From the values reported in Table V, we find that the function $\mathcal{F}$ in the integrand decays over a characteristic length scale of 100 nm, much greater than the spread of the localized wave function $\chi(\mathbf{r})$. Therefore, to a good approximation, we can substitute $\mathcal{F}(0) = 2/\pi$ to evaluate the integral. The final results for all phonon modes considered in Eqs. (25a) and (25b), and Eqs. (26a) and (26b) are obtained by a similar procedure.

APPENDIX E: FINITE-ELEMENT CALCULATION OF TWO BODY STATES IN HETEROBILAYER SYSTEM

The Schrödinger equation for two particles interacting through a radially symmetric potential $\mathcal{U}(r)$ is given by [6]

$$\left[-\frac{\hbar^2}{2m_1}\nabla_{\mathrm{e}}^2 - \frac{\hbar^2}{2m_2}\nabla_{\mathrm{h}}^2 - e^2\mathcal{U}(r_{12})\right]\Psi = E\Psi, \tag{E1}$$

where the form of the interaction $\mathcal{U}$ between charge carriers is explained in Appendix A 2, depending on the layer in which each particle is found.

Transforming the coordinates to the relative motion $\mathbf{r} = \mathbf{r}_1 - \mathbf{r}_2$ and the center-of-mass motion $\mathbf{R} = \frac{m_1\mathbf{r}_1 + m_2\mathbf{r}_2}{m_1+m_2}$ allows separation of the Schrödinger equation to the center-of-mass part whose solution is given by the plane wave $\phi(R) = \frac{1}{\sqrt{S}} e^{i\mathbf{K}\cdot\mathbf{R}}$ and the energy $E = \frac{\hbar^2 K^2}{2(m_1+m_2)}$, and the relative-motion part given by

$$\left[-\frac{\hbar^2}{2\mu}\nabla^2 - e^2\mathcal{U}(r)\right]\Psi = E\Psi, \tag{E2}$$

where $\mu = m_1 m_2/(m_1 + m_2)$ is the reduced mass.

Transforming the equation into dimensionless quantities [6,23] using the excitonic Bohr radius $a_0^* = \frac{\epsilon\hbar^2}{\mu e^2}$ and the excitonic Rydberg energy $R_{\mathrm{y}}^* = \frac{\mu e^4}{2\epsilon^2\hbar^2}$ gives

$$\left[-\tilde{\nabla}^2 - \frac{1}{R_{\mathrm{y}}^*}\mathcal{U}(a_0^*\tilde{r})\right]\Psi = \tilde{E}\Psi. \tag{E3}$$

where $\tilde{r} = r/a_0^*$ and $\tilde{E} = E/R_{\mathrm{y}}^*$. Using separation of variables the general solution is given by

$$\Psi(\mathbf{r}) = R(r)\Phi(\phi), \tag{E4}$$

where the angular-part solution is

$$\Phi(\phi) = \frac{1}{\sqrt{2\pi}} e^{il\phi}. \tag{E5}$$

$l = 0, \pm1, \pm2, \ldots$ is the azimuthal quantum number with $\Phi(\phi)$ being an eigenfunction of the angular momentum operator $L_z = -i\hbar\frac{\partial}{\partial\phi}$ with eigenvalue $\hbar l$. The equation for the radial part is

$$-R''(\tilde{r}) - \frac{1}{\tilde{r}}R'(\tilde{r}) + \frac{l^2}{\tilde{r}^2}R(\tilde{r}) - \tilde{v}(\tilde{r})R(\tilde{r}) = \tilde{E}R(\tilde{r}), \tag{E6}$$

where $\tilde{v}(\tilde{r}) = \mathcal{U}(a_0^*\tilde{r})/R_{\mathrm{y}}^*$. To solve Eq. (E6) numerically, we use the substitution $u(\tilde{r}) = R(\tilde{r})\tilde{r}$, allowing us to impose Dirichlet boundary conditions: $u(\tilde{r}) = 0$ at $\tilde{r} = 0$ and $\tilde{r} = \infty$. The equation can be solved using the finite-element method implemented in MATHEMATICA [53]. For the charged donor interacting with an electron in the $MoSe_2$ layer, we have $\mu = m_c'$, and we solve Eq. (E6) using both the approximate Keldysh interaction and the full bilayer potential for the intralayer interaction between the donor and electron. The normalized probability distributions for the first two radially symmetric states $(1s, 2s)$ obtained using both potentials are plotted in Fig. 11.

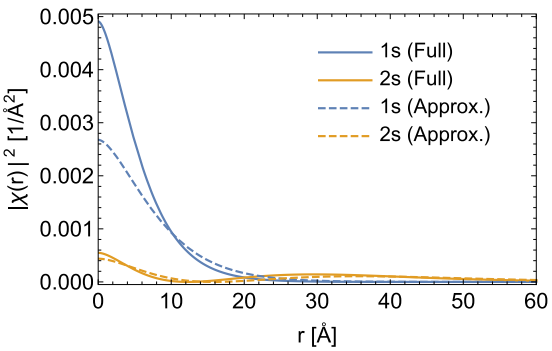

FIG. 11. Probability distributions ($|\chi(r)|^2$) of the first two radially symmetric donor atom states in hBN/$MoSe_2$/WSe_2/hBN. The solid lines were obtained using the full bilayer potential Eq. (1a), and correspond to states with binding energies $\mathcal{E}^{\mathrm{b}}_{1\mathrm{s}} = -229.03$ meV and $\mathcal{E}^{\mathrm{b}}_{2\mathrm{s}} = -61.73$ meV. The dashed lines were obtained using the approximate intralayer Keldysh form (A12).

[1] A. K. Geim and I. V. Grigorieva, Nature (London) **499**, 419 (2013).

[2] K. S. Novoselov, A. Mishchenko, A. Carvalho, and A. H. Castro Neto, Science **353**, aac9439 (2016).

[3] W. Zhang, Q. Wang, Y. Chen, Z. Wang, and A. T. S. Wee, 2D Mater. **3**, 022001 (2016).

[4] M. M. Furchi, A. Pospischil, F. Libisch, J. Burgdörfer, and T. Mueller, Nano Lett. **14**, 4785 (2014).

[5] C.-H. Lee, G.-H. Lee, A. M. van der Zande, W. Chen, Y. Li, M. Han, X. Cui, G. Arefe, C. Nuckolls, T. F. Heinz, J. Guo, J. Hone, and P. Kim, Nat. Nanotechnol. **9**, 676 (2014).

[6] M. Szyniszewski, E. Mostaani, N. D. Drummond, and V. I. Fal'ko, Phys. Rev. B **95**, 081301 (2017).

[7] A. T. Hanbicki, M. Currie, G. Kioseoglou, A. L. Friedman, and B. T. Jonker, Solid State Commun. **203**, 16 (2015).

[8] T. Cao, G. Wang, W. Han, H. Ye, C. Zhu, J. Shi, Q. Niu, P. Tan, E. Wang, B. Liu, and J. Feng, Nat. Commun. **3**, 887 (2012).

[9] X. Xu, W. Yao, D. Xiao, and T. F. Heinz, Nat. Phys. **10**, 343 (2014).

[10] C. Gong, H. Zhang, W. Wang, L. Colombo, R. M. Wallace, and K. Cho, Appl. Phys. Lett. **103**, 053513 (2013).

[11] J. Kang, S. Tongay, J. Zhou, J. Li, and J. Wu, Appl. Phys. Lett. **102**, 012111 (2013).

[12] P. Rivera, J. R. Schaibley, A. M. Jones, J. S. Ross, S. Wu, G. Aivazian, P. Klement, K. Seyler, G. Clark, N. J. Ghimire, J. Yan, D. G. Mandrus, W. Yao, and X. Xu, Nat. Commun. **6**, 6242 (2015).

[13] P. Nagler, G. Plechinger, M. V. Ballottin, A. Mitioglu, S. Meier, N. Paradiso, C. Strunk, A. Chernikov, P. C. M. Christianen, C. Schüller, and T. Korn, 2D Mater. **4**, 025112 (2017).

[14] E. M. Alexeev, A. Catanzaro, O. V. Skrypka, P. K. Nayak, S. Ahn, S. Pak, J. Lee, J. I. Sohn, K. S. Novoselov, H. S. Shin, and A. I. Tartakovskii, Nano Lett. **17**, 5342 (2017).

[15] H. Yu, Y. Wang, Q. Tong, X. Xu, and W. Yao, Phys. Rev. Lett. **115**, 187002 (2015).

[16] D. M. Ceperley and B. J. Alder, Phys. Rev. Lett. **45**, 566 (1980).

[17] W. M. C. Foulkes, L. Mitas, R. J. Needs, and G. Rajagopal, Rev. Mod. Phys. **73**, 33 (2001).

[18] F. Vialla and F. Koppens (private communication).

[19] L. V. Keldysh, JETP Lett. **29**, 658 (1979).

[20] B. Ganchev, N. Drummond, I. Aleiner, and V. Fal'ko, Phys. Rev. Lett. **114**, 107401 (2015).

[21] T. C. Berkelbach, M. S. Hybertsen, and D. R. Reichman, Phys. Rev. B **88**, 045318 (2013).

[22] M. Van der Donck, M. Zarenia, and F. M. Peeters, Phys. Rev. B **96**, 035131 (2017).

[23] E. Mostaani, M. Szyniszewski, C. H. Price, R. Maezono, M. Danovich, R. J. Hunt, N. D. Drummond, and V. I. Fal'ko, Phys. Rev. B **96**, 075431 (2017).

[24] A. Ramasubramaniam, Phys. Rev. B **86**, 115409 (2012).

[25] K. F. Mak, K. He, C. Lee, G. H. Lee, J. Hone, T. F. Heinz, and J. Shan, Nat. Mater. **12**, 207 (2012).

[26] J. S. Ross, S. Wu, H. Yu, N. J. Ghimire, A. M. Jones, G. Aivazian, J. Yan, D. G. Mandrus, D. Xiao, W. Yao, and X. Xu, Nat. Commun. **4**, 1474 (2013).

[27] Y. Lin, X. Ling, L. Yu, S. Huang, A. L. Hsu, Y.-H. Lee, J. Kong, M. S. Dresselhaus, and T. Palacios, Nano Lett. **14**, 5569 (2014).

[28] Y. Yu, S. Hu, L. Su, L. Huang, Y. Liu, Z. Jin, A. A. Purezky, D. B. Geohegan, K. W. Kim, Y. Zhang, and L. Cao, Nano Lett. **15**, 486 (2015).

[29] H. Wang, C. Zhang, W. Chan, C. Manolatou, S. Tiwari, and F. Rana, Phys. Rev. B **93**, 045407 (2016).

[30] M. Koshino and P. Moon, J. Phys. Soc. Jpn. **84**, 121001 (2015).

[31] Y. Wang, Z. Wang, W. Yao, G.-B. Liu, and H. Yu, Phys. Rev. B **95**, 115429 (2017).

[32] A. Kormányos, G. Burkard, M. Gmitra, J. Fabian, V. Zólyomi, N. D. Drummond, and V. Fal'ko, 2D Mater. **2**, 022001 (2015).

[33] R. Geick, C. H. Perry, and G. Rupprecht, Phys. Rev. **146**, 543 (1966).

[34] M. F. Plass, W. Fukarek, A. Kolitsch, N. Schell, and W. Möller, Thin Solid Films **305**, 172 (1997).

[35] K.-L. Barth, W. Fukarek, H.-P. Maucher, M. F. Plass, and A. Lunk, Thin Solid Films **313**, 697 (1998).

[36] S. L. Rumyantsev, M. E. Levinshtein, A. D. Jackson, S. N. Mohammad, G. L. Harris, M. G. Spencer, and M. Shur, in *Properties of Advanced Semiconductor Materials GaN, AlN, InN, BN, SiC, SiGe*, edited by M. E. Levinshtein, S. L. Rumyantsev, and M. S. Shur (Wiley, New York, 2001), Chap. 4, pp. 67–92.

[37] D. Xiao, G.-B. Liu, W. Feng, X. Xu, and W. Yao, Phys. Rev. Lett. **108**, 196802 (2012).

[38] A. Kumar and P. Ahluwalia, Physica B: Condens. Matter **407**, 4627 (2012).

[39] B. Amin, N. Singh, and U. Schwingenschlögl, Phys. Rev. B **92**, 075439 (2015).

[40] M. Danovich, I. L. Aleiner, N. D. Drummond, and V. I. Fal'ko, IEEE J. Sel. Top. Quantum Electron. **23**, 168 (2017).

[41] Z. Jin, X. Li, J. T. Mullen, and K. W. Kim, Phys. Rev. B **90**, 045422 (2014).

[42] X. Gu and R. Yang, Appl. Phys. Lett. **105**, 131903 (2014).

[43] K. Kaasbjerg, K. S. Thygesen, and A.-P. Jauho, Phys. Rev. B **87**, 235312 (2013).

[44] https://dx.doi.org/10.17635/lancaster/researchdata/219.

[45] H. Ogata, Publ. Res. Inst. Math. Sci. **41**, 949 (2005).

[46] N. D. Drummond, M. D. Towler, and R. J. Needs, Phys. Rev. B **70**, 235119 (2004).

[47] P. López Ríos, P. Seth, N. D. Drummond, and R. J. Needs, Phys. Rev. E **86**, 036703 (2012).

[48] T. Kato, Comm. Pure Appl. Math. **10**, 151 (1957).

[49] C. J. Umrigar, K. G. Wilson, and J. W. Wilkins, Phys. Rev. Lett. **60**, 1719 (1988).

[50] N. D. Drummond and R. J. Needs, Phys. Rev. B **72**, 085124 (2005).

[51] C. J. Umrigar, J. Toulouse, C. Filippi, S. Sorella, and R. G. Hennig, Phys. Rev. Lett. **98**, 110201 (2007).

[52] R. J. Needs, M. D. Towler, N. D. Drummond, and P. López Ríos, J. Phys. Condens. Matter **22**, 023201 (2010).

[53] *Mathematica, Version 11.0.1* (Wolfram Research, Inc., Champaign, Illinois, USA, 2016).

[54] F. Ceballos, M. Z. Bellus, H.-Y. Chiu, and H. Zhao, ACS Nano **8**, 12717 (2014).

[55] Y. Gong, J. Lin, X. Wang, G. Shi, S. Lei, Z. Lin, X. Zou, G. Ye, R. Vajtai, B. I. Yakobson, H. Terrones, M. Terrones, B. K. Tay, J. Lou, S. T. Pantelides, Z. Liu, W. Zhou, and P. M. Ajayan, Nat. Mater. **13**, 1135 (2014).